工學博士學位論文

Fabrication of Functionalized SiO_2/TiO_2 Hollow Nanoparticles for Drug Delivery and Neuronal Development Applications

기능성 실리카-티타니아 중공구조 나노 입자의 제조 및 약물전달과 세포분화에서의 응용

2017年 2月

서울大學校 大學院

化學生物工學部

張 允 宣

Fabrication of Functionalized SiO_2/TiO_2 Hollow Nanoparticles for Drug Delivery and Neuronal Development Applications

by

Yoonsun Jang

Submitted to the Graduate School of Seoul National University in Partial Fulfillment of the Requirements for the Degree of Doctor of Philosophy

February, 2017

Thesis Adviser: Jyongsik Jang

Abstract

In recent years, to incorporate diverse components into a single nanoscale system have been a great deal of interest in biomedical fields. These hybrid nanomaterials provide multifunctionality and the extraordinarily enhanced performance than bulk sized material- or single component nanomaterial-based application. Therefore, with advancing in nanotechnology, many efforts have been also paid to the fabrication of hybrid materials. Nanoparticle is the basic structure to achieve such hybridiziation. Additionally, nanoparticle is the most internalized structure in the cells compared to other nanostructures. However, there is still lack of literature about fabrication of hybrid nanoparticles for biomedical applications.

The dissertation describes the fabricating multifunctional hybrid nanoparticles, evaluating their cytotoxicity, and applying them into neuronal development promoter, stimuli responsive anticancer therapy. This dissertation describes the different ways in the synthetic methology of hybrid nanoparticles. First, GO enwrapped HNPs were fabricated for PpIX loading agent and employed for PDT and PTT agent. In case of both of NIR and visible light irradiation condition, the PTT and PDT synergic therapeutic effect has been attained. Second, Mg-HNP, Ca-HNP, Sr-HNP, and Ba-HNPs were used to encapsulating agent for nerve growth factor and further applied as neuronal differentiation enhancer. Sr-HNPs were exceptionally efficient for promoting neuronal development cooperated with nerve growth factor. Third, a stimuli-responsive

GQD/PPy-HNPs were synthesized for use as a bio imaging and drug delivery agent. Each hybrid nanoparticles are intentionally designed and customized of superior performance in specific performance.

This dissertation provides the possibility of various approaches for the preparation of multifunctional hybrid nanoparticles and their biomedical applications. The hybrid nanoparticles presented in the dissertiation could be applied into biomedical fields such as neuronal development promoter, enhanced phototherapy agent, bioimaging probe, and controlled drug release system. This study might provide understanding of fabricating hybrid nanoparticles with multifunctionality and application of hybrid nanoparticles to biomedical application.

Keywords: Hybrid nanoparticle; Cytotoxicity; Neuronal development; Drug delivery; Bioimaging
Student Number: 2014-30296

List of Abbreviations

$^1O_2$: Singlet oxygen

ABDA: 9,10-anthracenediyl-bis(methylene) dimalonic acid

AFM: Atomic Force Microscope

APTES: (3-Aminopropyl)triethoxysilane

$Ba(OH)_2$: barium hydroxide

BET: Brunauer-Emmett-Teller

BSA: bovine serum albumin

$Ca(OH)_2$: calcium hydroxide

ca.: circa

Ce6: Chlorin e6

CO_2: carbon dioxide

CSNP: core-shell nanoparticle

DAPI: 4,6-diamidino-2-phenylindole dihydrochloride

DEX: dexamethasone

DMSO: dimethyl sulfoxide

DNA: deoxyribonucleic acid

EDS: Energy Dispersive X-ray Spectroscopy

eV: electron volt

FACs: fluorescence activated cell sorter

$FeCl_3$: iron (III) chloride

FE-SEM: field emission-scanning electron microscopy

FITC: Fluorescein isothiocyanate

FT-IR: Fourier transform infrared

GO: graphene oxide

GQD: graphene quantumdot

H2O2: hydrogen peroxide

HA: hyaluronic acid

HBSS: Hank's Balanced Salt Solution

HNP: hollow nanoparticle

HR-TEM: high resolution-transmission electron microscopy

I-V: current-voltage

M: mole

MCF-7: Michigan Cancer Foundation-7

$Mg(OH)_2$: magnesium hydroxide

mM: milli mole

MRI: magnetic resonance imaging

N_2: nitrogen

NGF: nerve growth factor

NH_3OH: ammonium hydroxide solution

NIR: near infrared

nm: nano meter

nM: nano mole

PBS: phosphate buffered

PDT: Photodynamic therapy

PEG: Polyethylene glycol

pH: hydrogen exponent

pHis: Polyhistidine

PI: propidium iodide

PL: Photoluminescence

PpIX: protoporphyrinIX

PPy: polypyrrole

PS: photosensitizer

Pt: platinum

Rh-123: Rhodamine-123

ROS: reactive oxygen species

s: second

SiO_2: silica

SMER: sonication mediated etching and redeposition

SOG: singlet oxygen generation

$Sr(OH)_2$: strontium hydroxide

TAT: Trans-Activator of Transcription

TEM: Transmission electron microscopy

TEOS: Tetraethyl orthosilicate

TEOS: tetraethyl orthosilicate

TiO_2: titania

TTIP: titanium (IV) isopropoxide

UV-Vis light: ultraviolet-visible light

V: voltage

XPS: x-ray photoemission spectroscopy

μm: micro meter

List of Figures

NIR laser irradiation and b) with NIR laser irradiation were observed with different time scale by using visible light. The change of absorption intensity of ABDA c) with NIR and d) without NIR irradiated GO-HNP-PpIX nanoparticles. (black: with irradiation, white: without irradiation). Values exhibit mean ± SD, and each experiment was performed in triplicate.

Figure 21. Photobleaching of ABDA (0.07 mg mL^{-1}, 3 mL) by HNP-PpIX (0.3 mg mL^{-1}) nanoparticles dispersed in 0.1 M PBS. Absorbance spectra of HNP-PpIX nanoparticles in a condition of a) without 808 nm laser irradiation and b) with 808 nm laser irradiation were observed with different time scale by using visible light. The change of absorption intensity of ABDA c) with NIR and d) without NIR irradiated HNP-PpIX nanoparticles. (black: with irradiation, white: without irradiation). Values exhibit mean ± SD, and each experiment was performed in triplicate.

Figure 22. TEM images of particle-internalized MCF-7 cells incubated with a) HNPs, b) GO-HNP, c) GO-HNP-PpIX without NIR irradiation, and d) GO-HNP-PpIX with 0.8 W cm-2 of NIR irradiation. (MCF-7 cells were incubated at the equivalent 25 μg mL^{-1} HNP concentration). Right: magnified images of a), b), c), and d). (red arrows indicate the

Figure 27. Livecell fluorescence images of MCF-7 cells treated with 100 μg mL^{-1} of a) no particle (control), b) GO-HNP, c) HNP-PpIX, and d) GO-HNP-PpIX. Cells were stained with DeadEnd™ Fluorometric TdT-mediated dUTP Nick-End Labeling (DeadEnd™ Fluorometric TUNEL) assay and Fluoroshield™ with 4′,6-Diamidino-2-phenylindole dihydrochloride (Fluoroshield™ with DAPI) for visualing viable and dead cells. Each fluorescent images were taken at the same time (scale bars: 100 μm).

Figure 28. Livecell fluorescence images of MCF-7 cells treated with 100 μg mL^{-1} of GO-HNP-PpIX. From left to right, the visible light irradiation time is a) 0 miin, b) 5 min, c) 10 min, and d) 15 min with fixed 0.8 W cm-2 of NIR laser irradiation. Cells were stained with DeadEnd™ Fluorometric TdT-mediated dUTP Nick-End Labeling (DeadEnd™ Fluorometric TUNEL) assay and Fluoroshield™ with 4′,6-Diamidino-2-phenylindole dihydrochloride (Fluoroshield™ with DAPI) for visualing viable and dead cells. Each fluorescent images were taken at the same time (scale bars: 100 μm).

Figure 29. Livecell fluorescence images of MCF-7 cells treated with 100 μg mL^{-1} of HNP-PpIX. From left to right, the visible light irradiation time is a) 0 miin, b) 5 min, c) 10 min, and d) 15 min with 0.8 W cm-2 of 808

nm laser irradiation. Cells were stained with DeadEnd™ Fluorometric TdT-mediated dUTP Nick-End Labeling (DeadEnd™ Fluorometric TUNEL) assay and Fluoroshield™ with 4′,6-Diamidino-2-phenylindole dihydrochloride (Fluoroshield™ with DAPI) for visualing viable and dead cells. Each fluorescent images were taken at the same time (scale bars: 100 μm).

Figure 30. a) ROS generation and b) mitochondrial dysfuction of MCF-7 cells after incubation with 100 μg mL^{-1} concentration of GO-HNP-PpIX for 24 h. After incubation of GO-HNP-PpIX, cells were irradiated for different time scale 0 min, 5 min, 10 min, and 15 min (1.5 % H_2O_2 treated MCF-7 cells were used as positive control). Values exhibit mean ± SD and each experiment was performed in triplicate. *Statistically significant difference from negative control

Figure 31. Illustrative diagram of fabrication process of the alkaline earth metal ion-doped hollownanoparticle (HNP) for encapsulating nerve growth factor (NGF).

Figure 32. TEM images of a) Mg-HNPs, b) Ca-HNPs, c) Sr-HNPs, and d) Ba-HNPs. (below: size distribution of HNPs).

Figure 33. Doping and etching of Mg-HNPs, Ca-HNPs, Sr-HNPs, and Ba-HNPs as a function of treatment time. Under sonication, alkaline earth metal

time is 0, 1000, and 5000 μg mL^{-1}. Cells were stained with propidium iodide (PI) for visualing necrosis of cells. DIC images were taken at the same time, corresponding to the fluorescence images (scale bars: 100 μm).

Figure 52. a) Cell viability and b) ROS generation of the MCF-7 cells treated with DEX solution released from HNP, PPy-HNP, and GQD/PPy-HNP. The experiments were conducted with cycle time. Cells were stimulated after 24 h incubation of nanoparticles. Values exhibit mean ± SD and each experiment was performed in triplicate.

List of Tables

Table of Contents

1. Introduction

1.1 Background

1.1.1 Nanomaterials

Nanomaterials are defined as materials with at least one external dimension in the size range from about 1-100 nanometers (**Figure 1**).

Nanoparticles that are naturally occurring or are the incidental byproducts of combustion processes are usually physically and chemically heterogeneous and often termed ultrafine particles. Nanoparticles can be precisely designed and intentionally produced with very specific properties related to shape, size, surface properties and chemistry (**Figure 2**). These properties are reflected in aerosols, colloids, or powders. Often, the behavior of nanomaterials may depend more on surface area than particle composition itself. Relative-surface area is one of the principal factors that enhance its reactivity, strength and electrical properties, etc.

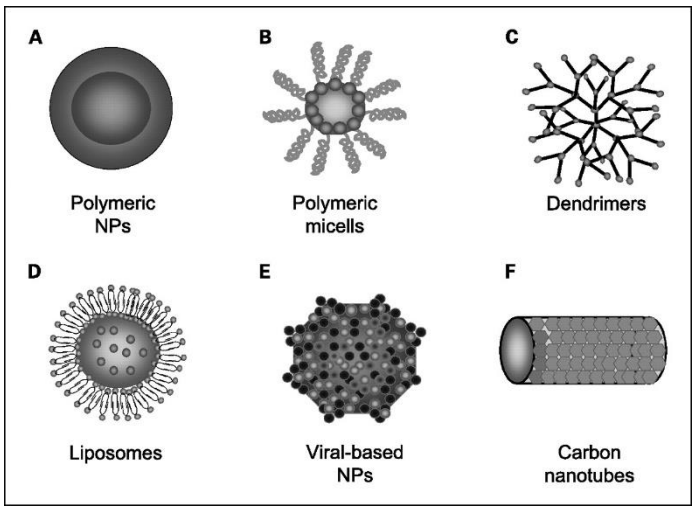

Figure 1. Types of nanocarriers for drug delivery. A, polymeric nanoparticles: polymeric nanoparticles in which drugs are conjugated to or encapsulated in polymers. B, polymeric micelles: amphiphilic block copolymers that form to nanosized core/shell structure in aqueous solution. The hydrophobic core region serves as a reservoir for hydrophobic drugs, whereas hydrophilic shell region stabilizes the hydrophobic core and renders the polymer to be water-soluble. C, dendrimers: synthetic polymeric macromolecule of nanometer dimensions, which is composed of multiple highly branched monomers that emerge radially from the central core. D, liposomes: self-assembling structures composed of lipid bilayers in which an aqueous volume is entirely enclosed by a membranous lipid bilayer. E, viral-based nanoparticles: in general structure are the protein cages, which are multivalent, self-assembles structures. F, carbon nanotubes: carbon cylinders composed of benzene rings [1].

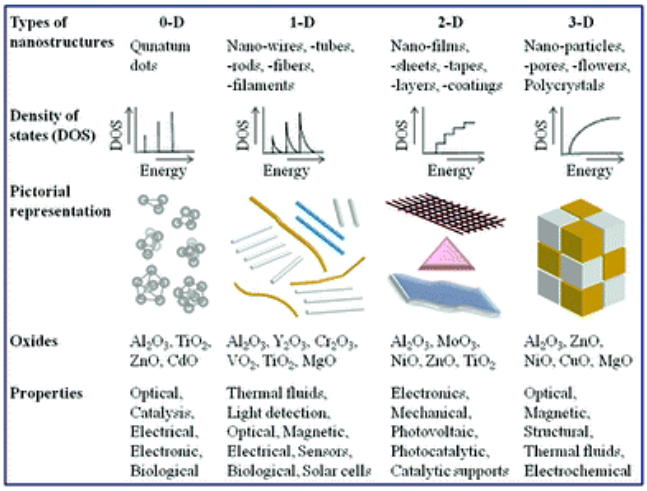

Figure 2. Classification of nanomaterials by shape.[2]

1.1.1.1 Unique properties of nanomaterials

The unique properties of the various types of nanomaterials give them novel electrical, catalytic, magnetic, mechanical, thermal, or imaging features that are highly desirable for applications in bioimaging agents, sensors, biomedical agents, and photovoltaic devices in **Figure 3**. These materials may also find their way into more complex nanostructures and systems. As compare to conventional bulk particles nanomaterials exhibits some unique physical properties including electrical, catalytic, magnetic, mechanical, thermal, or imaging features that make the nanomaterials a relevant topic in many materials science. The nanomaterial possesses some remarkable and specific peculiar properties which may be significantly distinctive from the physical properties of bulk materials. As a matter of fact, nanomaterials have unique properties relative to bulk counterpart which impart them beneficial characteristics; they may garnered them with unique mechanisms of toxicity. In general, toxicity has been thought to originate from nanomaterials' size and surface area, composition, shapes. In this thesis, I precisely regulate the nanomaterials to obtain low cell toxicity. To synthesize the useful

nanomaterials with endowing low cell toxicity, we facilitate the inorganic SiO_2/TiO_2 nanocomposites with uniform spherical structure.

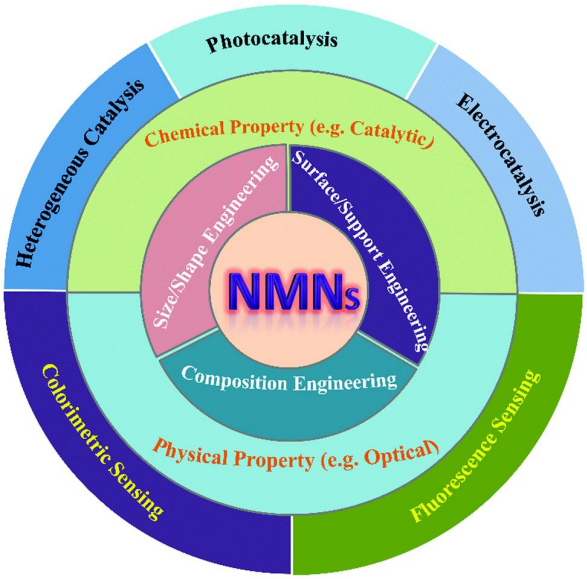

Figure 3. Various application area of nanomaterials [3].

1.1.1.2 Synthesis and characteristics of inorganic nanoparticles

Over the last few years, interest in the synthesis and properties of colloidal inorganic particles has steadily grown because of the great expectations for their application in different fields of material science and technology [4]. This is due to their unique properties: catalytic, optical, semiconductive, magnetic, antifriction and others. Indeed, the variation of size of metal nanoparticles provides the regulation of catalytic properties, mainly changing their activity, while nature of nanoparticle environment can influence both activity and selectivity of the catalytic species [5].

In **Figure 4**, a different kinds of methods for the preparation and stabilization of nanoparticles exists in the literature, including formation of inorganic nanoparticles in reverse microemulsion environment in polymeric systems, by vapor-phase procedures, by thermal decomposition, of organometallic precursors and so on [6].

Most of unique and advanced properties are inherent to bare nanoparticles of metals and semiconductor compounds. Bare nanoparticles usually possess excessive surface energy and should be protected (surface capping or modification) or placed in an inert matrix

for use in most applications [7]. Unprotected inorganic nanoparticles in liquid media are thermodynamically unstable with respect to growth, and they tend to spontaneously coalescence and usually the nanoparticle surface is passivated by suitable capping reagents, i.e. electron donors or acceptors species that bond to the nanoparticle surface [8, 9]. These coatings provide stabilization of nano-sized objects in viscous liquid or semi-liquid media, such as polymeric matrixes, micelles, and aerogels (**Figure 5**) [10].

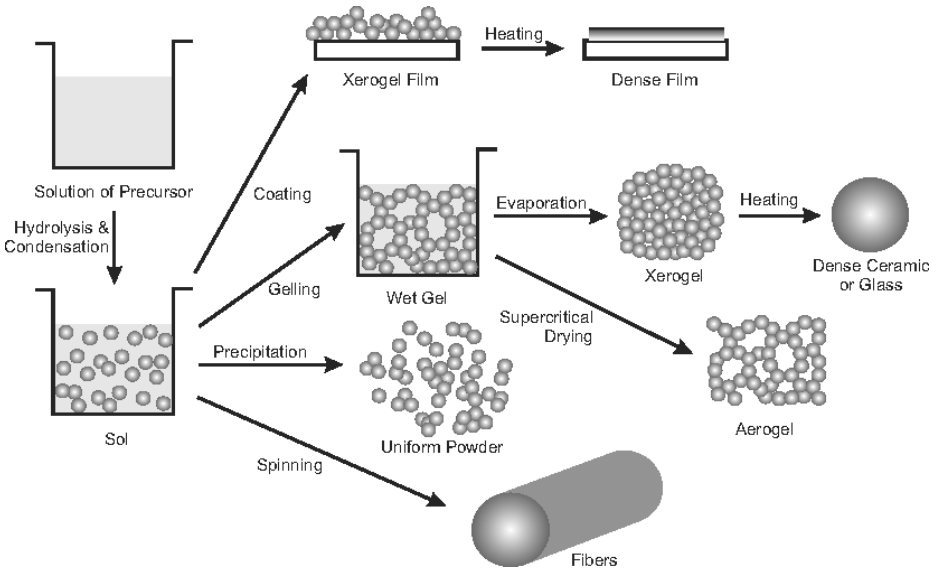

Figure 4. Variety of methods for the preparation and stabilization of nanoparticles [10].

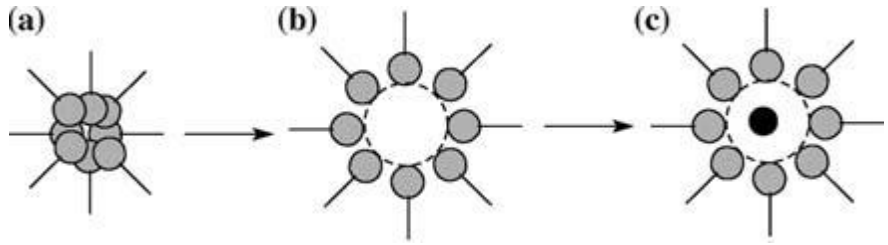

Figure 5. Emulsion polymerization process. Solvent mixture isooctane;chloroform, surfactant; hexadecyltrimethylammonium bromide, CTAB [11]

1.1.1.3 Functionalities and applications

The use of nanomaterials in technological applications is limited because of their restricted behavior in different environmental condition. Molecular engineering on the surfaces of nanoparticle helps the nanomaterials to tune their properties which plays a vital role in exploring and developing their applications in the field of nanotechnology [12].

The surface properties of nanoparticles determine the interaction among the components, as well as the solubility and agglomeration behavior in different solvents and thus, decide whether individual nanocrystals are stable as nanomaterial blocks [13]. Moreover, the surface modifying groups of the nanoparticles can be used to couple the unique electronic, photonic, or catalytic properties of quantum-size nanoparticles with molecular or macromolecular functionalities to yield hybrid systems with advanced features. For example, in **Figure 6**. nucleic acid-functionalized Au nanoparticles, exhibiting a characteristic red color originating from the single-particle plasmon exciton, turns blue upon hybridization with the target DNA due to the formation of an interparticle-coupled plasmon exciton.

Furthermore, there are different approaches to modify the surfaces of inorganic nanomaterials to make organic-inorganic nanocomposites. The simplest approach is to entrap an inorganic component in an organic host. Examples include inorganic-organic hybrid polymers with interpenetrating but otherwise nonconnected inorganic and organic networks, polymers filled with inorganic nanoparticles, or layered inorganic compoundes interclated with organic molecules.

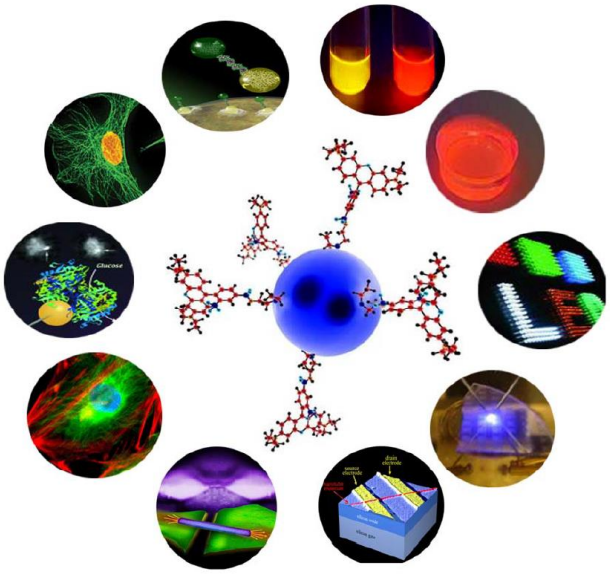

Figure 6. Use of functionalized nanoparticles in various fields of nanotechnology [14].

1.1.2 Nanoparticles for Biomedical applications

Nanoparticles in nanosize have significantly different characteristics from particles which is not included in nanoscale (1-100 nm). Since these nanoparticle properties are often in many applications, they have been applied in a wide variety of research [15-17]. Popular nanoparticles in biomolecular and biomedical imaging include fluorescent particles for optical imaging, such as quantum dots, gold nanoparticles and magnetic particles. Nanoparticle derives therapeutics includes heat ablation of target tumours, or delivery of drugs. **Figure 7** and **Figure 8** summarizes the attributes of multifunctional nanoparticles that have attracted the field of bioimaging and medicine. Multiple modalities of these particles enable the accurate, less-invasive diagnosis and therapeutic approaches.

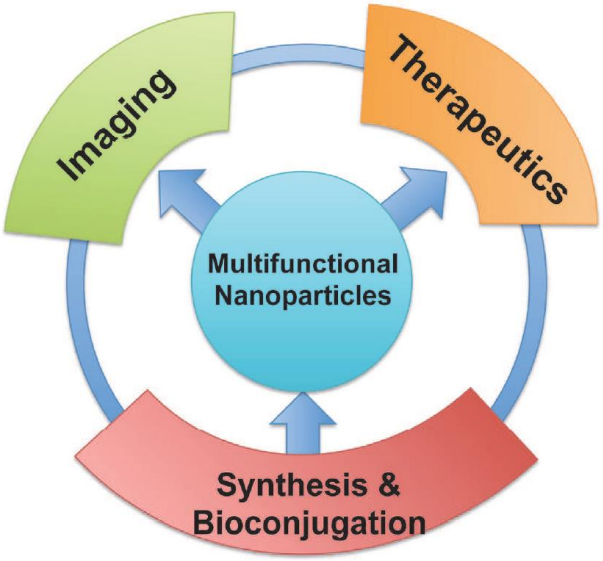

Figure 7. Multifunctional nanoparticles in bioimaging and medicine. Developed synthesis and bioconjugation strategies for multifunctional nanoparticles helps enabling applications of multifunctional nanoparticles in in vivo imaging and therapy [18].

Figure 8. Diagram representing the possible bio-medical applications of carbon-coated magnetic nanoparticles [19].

1.1.2.1 Phototherapy application

The phototherapy are divided as following categories: 1) Photodynamic therapy (PDT) and 2) Photothermal therapy (PTT). In PDT system, the singlet oxygen has been exploited for eliminate malignant cells. The singlet oxygen ($^1O_2$), as a part of reactive oxygen species (ROS) is useful tool to destruct cancer cells at the local site when singlet oxygen is concentrated. PDT is a new technology to treat tumor based on nanoparticle generated ROS at the tumor site [20]. In **Figure 9**, the photosensitizers (PS), such as nanoparticles, can produce ROS when they are activated with the appropriate wavelength of excitation light. Nanoparticles as photosensitizers must be in close proximity to the tumor cells that they are usually administered at the tumor site directly. Photodynamic therapy is desirable in that it is relatively non-invasive and low toxicity. The major technical barrier, however, of this therapy is its difficulty in systemic introduction of photosensitizer to the tumor site and local irradiation to activate them. The UV light is the wavelength of choice for the most of traditional photosensitizers that cannot efficiently penetrate into deep tissue. Therefore, the new class of nanoparticles was introduced to destroying the tumor site as well, exhibited as in **Figure 10**

[21]. Photo-responsive nanoparticles are excited by near infrared light that can efficiently penetrate tissues deeper than UV-VIS light, which allows for the non-invasive application of the method. Functionalized surface on nanoparticles can direct particles to the specific tumor site that will concentrate ROS production. The second part of phototherapy is so called PTT. PTT is a physical treatment by using near-infrared (NIR) light, in which light could be converted into cytotoxic heat to kill cancer cells and minimize the invasive damage to normal tissues and cells. In all of the light sources, NIR light with wavelengths ranging from 700 to 1100 nm possesses a long penetration depth up to several inches and has been widely applied for photothermal therapy owing to its minimal attenuation by blood and tissues [22].

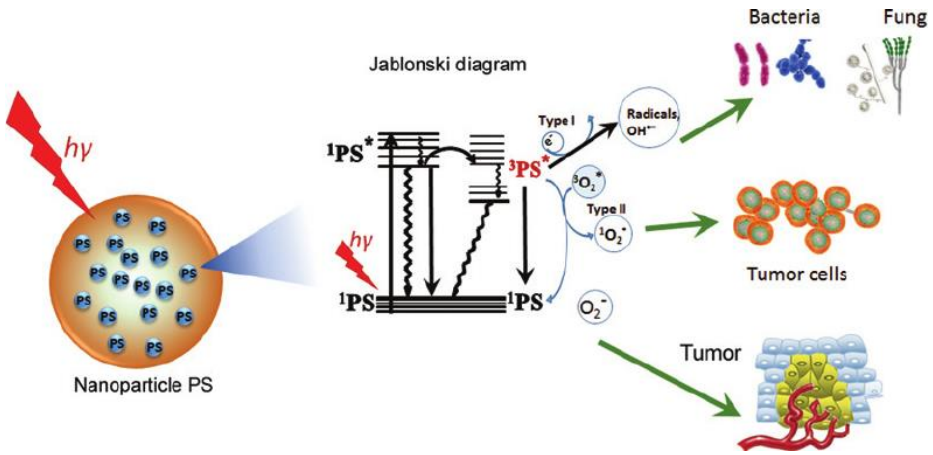

Figure 9. Jablonski diagram showing how nanoparticle-encapsulated PS can generate different ROS upon illumination that are able to kill pathogens and cancer cells and can also destroy tumors [23].

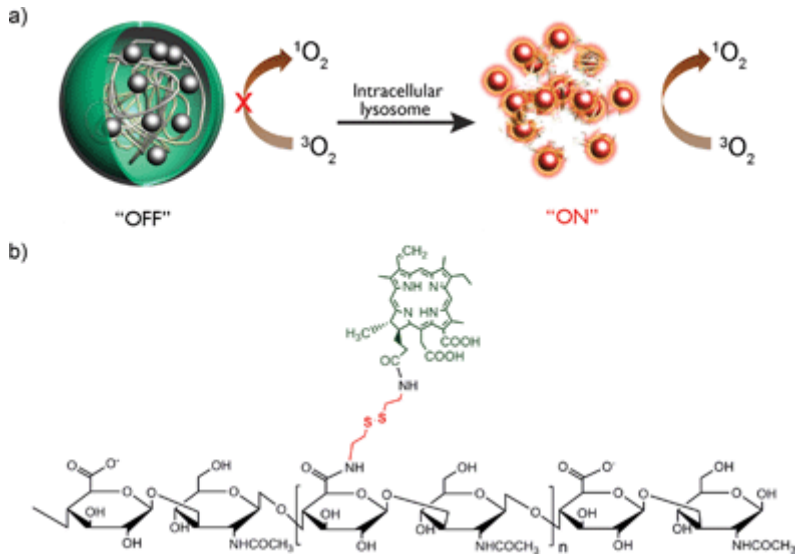

Figure 10. a) Schematic drawing of the redox-responsive nano-PDT agent. Fluorescence and singlet oxygen generation (SOG) are quenched in the native state. When the nanoparticles enter cancer cells *via* endocytosis, disulfide bonds are cleaved by intracellular reductive agents, resulting in dequenching of fluorescence and SOG. b) Chemical structure of the synthesized HA–Ce6 conjugate [24].

1.1.2.2 Stimuli-responsive drug release

On-demand drug delivery is becoming feasible through the design of stimuli-responsive systems that recognize their microenvironment and react in a dynamic way, mimicking the responsiveness of living organisms. However, this approach is rather complex. It requires the use of biocompatible materials that are able to undergo a specific protonation, a hydrolytic cleavage, or a molecular or supramolecular conformational change in response to a desired stimulus, or that are susceptible to specific physical stimulation. The concept of stimuli-responsive drug delivery was first suggested in the late 1970s with the use of thermosensitive liposomes for the local release of drugs through hyperthermia1. Since then a great deal of research has been carried out on stimuli-responsive materials for drug delivery, especially concerning their design and application as nanocarriers. In **Figure 12**, the nanoscale stimuli-responsive devices may be sensitive to specific endogenous stimuli, such as a lowered interstitial pH, a higher glutathione concentration or an increased level of certain enzymes such as matrix metalloproteinases. At the cellular level, pH sensitivity can either trigger the release of the transported drug into late endosomes or lysosomes. At

the tissue level, one can take advantage of specific microenvironmental changes associated with neoplastic diseases (the treatment of which is the focus of most of the research effort on stimuli-responsive nanocarriers) as well as pathological situations such as ischemia, inflammatory diseases or infections. For example, the targeted delivery of pharmacologically active molecules to a diseased area in the body can be magnetically guided by using ultrasmall iron oxide-based nanoparticles. Sustained drug release can also be achieved by thermo-, light- or ultrasound-sensitive nanoparticulate systems were presented in **Figure 12.**

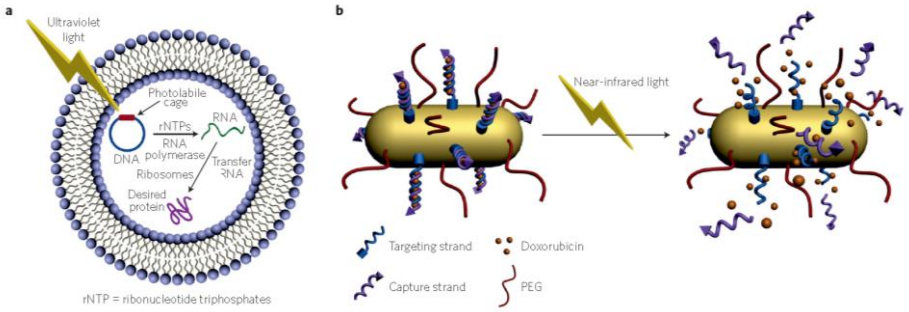

Figure 11. Examples of light-triggered drug delivery. a, Schematic representation of an encapsulated in vitro transcription–translation liposomal system triggered by irradiating caged DNA with light. b, Delivery of doxorubicin through the near-infrared-triggered induction of dehybridization of the DNA conjugated at the surface of gold nanorods [25, 26].

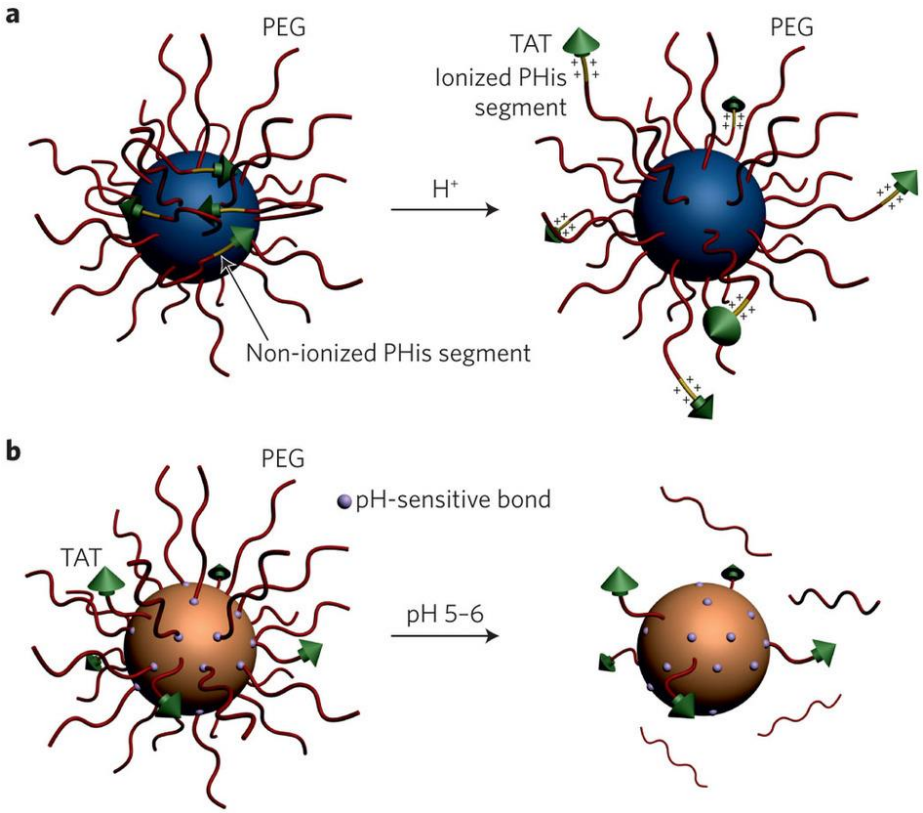

Figure 12. Polyhistidine (PHis)-based micelles responding to acidic tumour microenvironments by an efficient TAT-sequence exposure following ionization of the polyhistidine segments. b, TAT-peptide-decorated liposomes comprising a hydrolyzable PEG shell allowing improved exposure of the TAT sequence at low pH [27, 28].

1.1.2.3 Neural development promoter

The human brain is a complex network of more than 100 billion interconnected neurons [29]. These extraordinary cells are specialized in information processing and transmission by electrochemical signalling. A mammalian neuron consists of a cell body, called soma or perikaryon, and several cellular processes, called neurites. In **Figure 13** and **Figure 14**, the neurites are distinguished into multiple, widely ramified dendrites and one axon.

Neurons grow and function while sensing and responding to a wide range of chemical and physical environmental cues through the tips of their developing neurites. It has been recognized that neurons are highly influenced by the physical properties of substrates, including topography at the micro- and nano- scale [30-32]. The combination of physical and chemical stimulations by using active materials as the nanotopographic platform to promote neuronal regenerative response [33].

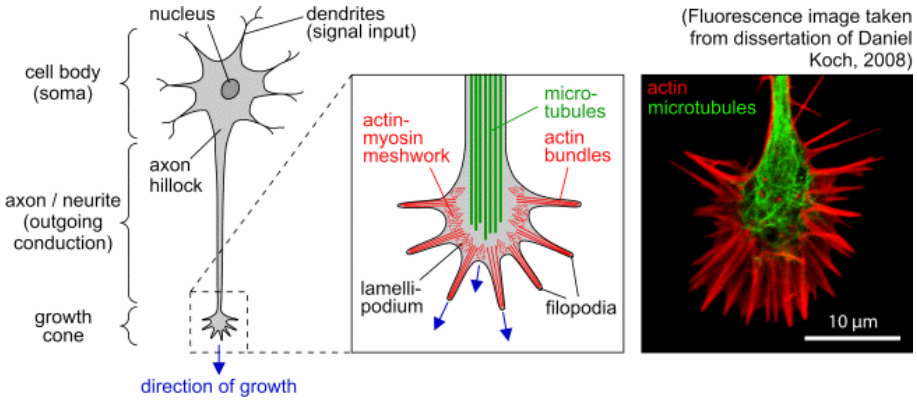

Figure 13. Schematic representation of a neuron and detailed view of the growth cone with its main cytoskeletal components (actin filaments and microtubules). The fluorescence image on the right-hand side shows an NG108 growth cone [34].

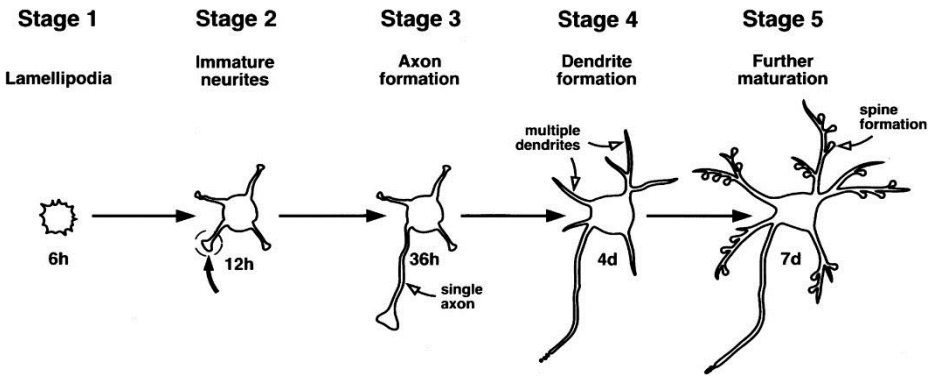

Figure 14. Establishment of polarity and stages of neuronal development in hippocampal neurons [35].

1.2 Objectives and Outlines

1.2.1 Objectives

The aim of this dissertation is proposing novel method to fabricate multi-functionalized hollow nanomaterials for evaluating their cytotoxicity and applying them into enhancement of neuronal differentiation and stimuli responsive drug release property. In particular, three types of silica-titania hollow nanoparticle based hybrid materials are fabricated by stöber and sol-gel method. They are employed for photosensitizer delivery agent, neuronal development enhancer, and controlled drug release system. In case of graphene oxide (GO) enwrapped nanoparticles were fabricated by solvent exchange method, silane coupling method, and charge-charge interaction for delivering photosensitizer selectively. In the second part, alkaline earth metal (AEM) doped SiO_2/TiO_2 hollow nanoparticles were fabricated using sonication mediated etching and redeposition (SMER) method. In cooperation with nerve growth factor (NGF), the fabricated AEM-HNPs were applied as neuronal development enhancer. In the third part, a dual functional nanoparticles were used as elecetical stimuli responsive drug delivery

agent and fluorescence probe. To obtain the multi-functionalization, we exploited the polypyrrole (PPy) and graphene quantum dot (GQD). The GQDs were embedded into the PPy nanoshell (GQD/PPy) and the GQD/PPy has been surface coater for HNP (GQD/PPy-HNP). Each hybrid nanoparticles are deliberately designed and customized for superior performance in drug delivery and neuronal development applications.

1.2.2 Outlines

In the view point of abovementioned topics, this dissertation involves the following subtopics:

I. GO wrapped hollow nanomaterials for phototherapy

I-1. Fabrication of GO wrapped hollow nanoparticles

I-2. Application for Phototherapy

II. Alkaline earth metal ion-doped hollow nanoparticles for neuron development

II-1. Fabrication of Alkaline earth metal ion-doped hollow nanoparticles

II-2. Application for Neuron development promoter

III. GQD/PPy coated hollow nanoparticles for bioimaging and drug delivery

III-1. Fabrication of GQD/PPy coated hollow nanoparticles

III-2. Application for Stimuli-responsive drug release

III-3. Application for Bioimaging system

2. Experimental Details

2.1 GO wrapped hollow nanomaterials for phototherapy

2.1.1 Fabrication of GO wrapped hollow nanoparticles

Synthesis of colloidal SiO_2 *via* Stöber method was first step in fabrication of SiO_2/ TiO_2 hollow nanoparticles. Tetraethyl orthosilicate (TEOS; Aldrich, St. Louis, MO, 2.9 mL) was added into solution of ethanol (78 mL) and ammonia solution (3.9 mL). The mixture solution was stirred for 12 h at 45°C. After the synthesis, 29 mL of acetonitrile was added to as-prepared colloidal SiO_2. Then, 3 mL of titanium (IV) isopropoxide (TTIP; Aldrich), 20 mL of ethanol, and 6 mL of acetonitrile were mixed. The mixed solution was reacted with the colloidal SiO_2 at 4°C for 12 h. To fabricate HNP, the resulting core-shell nanoparticle (CSNP) were treated with ammonia solution (0.1 M), for overnight. To load protoporphyrinIX (PpIX; Aldrich) into the HNPs, 50 mg of PpIX was added to the HNPs in DMSO (2mg mL^{-1}) After this PpIX loading procedure, the PpIX encapsulated HNPs were washed with water for three times to remove absorbed PpIX on the surface of the HNPs. The

0.5 mL of triethoxysilane (APTES; Aldrich) were dropped into ethanol solution with HNP-PpIX for overnight. Following, 5 mg of graphene oxide (GO) was added and stirred overnight. The solution was thoroughly washed to remove unreacted GO.

2.1.2 Characterization of GO wrapped hollow nanoparticles

Transmission electron microscopy (TEM) images were obtained with a JEOL EM-2000 EX II microscope. The size distribution of HNPs were measured by ELS-Z1000 (Otsuka Electronics, Japan). The BET surface area and average pore volume was analyzed by ASAP 2000 (Micromeritics, USA). Microscopic characterization and AFM topography analysis were carried out with a Digital Instruments Nanoscope IIIA from Veeco Systems in tapping mode using silicon tips with a resonance frequency of 320 kHz and a trigger threshold of 1.0 V. Fourier transform infrared (FTIR) spectra were obtained using a FT-IR Frontier (PerkinElmer, USA) in absorption mode at a resolution of 64 cm^{-1}. Ultraviolet-visible (UV-Vis) spectra were acquired using a Lambda-20 spectrometer (PerkinElmer, USA). Photoluminescent absorption spectra were gained with LS-55 spectrofluorometer (PerkinElmer, USA).

The synthesized GO-HNP-PpIX was diluted with phosphate buffered salin (PBS) (0.3 mg mL^{-1} of GO-HNP-PpIX). PpIX was released from GO-HNP-PpIX and detected by UV-vis spectrometry with 10 min of intervals. In each experiment, the GO-HNP-PpIX was centrifuged for

separating released PpIX from GO-HNP-PpIX. After the centrifugation, the supernatant was collected and the relative PpIX release % was calculated. The cumulative PpIX release % was calculated by Equation (1). Where mtotal is the total mass of PpIX and $m_{released}$ is a mass of released PpIX from GO-HNP-PpIX.

$$\text{PpIX release (\%)} = \frac{m_{released}}{m_{total}} \times 100 \quad (1)$$

To measure the photothermal effect of GO-HNP-PpIX, GO-HNP, HNP-PpIX, and GO-HNP-PpIX were dispersed in the 1 mL of the 0.1 M PBS (0.5 mg mL^{-1}). Each samples were irradiated using an 808 nm NIR laser with 2 min of interval. The temperature were recorded by using a Testo 925 thermomoter (Testo, Lenzkirch, Germany).

The loaded amount of PpIX was calculated as followings: First, at the HNP-PpIX fabrication process, the PpIX contained supernatant was collected and the residual PpIX amount was measured by UV-vis spectrometry. The drug loading capacity was calculated by Equation (2).

$$\text{Drug loading (\%)} = \frac{m_{total} - m_{residual}}{m_{HNP-PpIX}} \times 100 \quad (2)$$

Where m_{total} is the total mass of PpIX and $m_{residual}$ is a mass of residual PpIX in the supernatant. $m_{HNP\text{-}PpIX}$ is mass of PpIX loaded into HNPs.

The singlet oxygen ($^1O_2$) generated by PpIX was observed by photobleaching of the chemical $^1O_2$ probe 9,10-anthracenediyl-bis(methylene) dimalonic acid (ABDA; Aldrich). The reaction was monitored spectrophotometrically by recording the decrease in absorbance intensity at 380 nm. In a typical experiment for $^1O_2$ production measurement, GO-HNP, HNP-PpIX, and GO-HNP-PpIX nanoparticle solution (equivalent concentration of PpIX: 100 nM) in phosphate buffer (0.1 M, pH 7–7.4) was mixed with 10 μL of ABDA solution (50 μg mL^{-1}). The solution was irradiated with 0.8 W cm^{-2} of 808 nm NIR laser diode (Lilly Electronics, China) and 5.6 mW cm^{-2} LED light lantern (ING, China). The 808 nm NIR laser was irradiated for 5 min. Afterward, the visible light was irradiated to the samples with different time scale (0 min, 5 min, 10 min, and 15 min) and then the decrease in ABDA absorption was monitored by UV-visible spectrometer.

2.1.3 Application for Phototherapy

Human breast cancer MCF-7 cell line was purchased from ATCC American type culture collection). The cellular uptake of HNP, GO-HNP, and GO-HNP-PpIX upon MCF-7 cells were observed by using transmission electron microscopy (TEM). The cells were seeded in culture dishes (Nunc, Thermo Fisher Scientific, USA) and cultivated for 24 h at a density of 1×10^5 cells mL^{-1}. After add the HNPs, GO-HNP, and GO-HNP-PpIX solutions (incubated with equivalent 25 mg mL^{-1} of HNPs) to the cells for 24 h, cells were rinsed with 0.1 M HBSS to eliminate floating nanoparticles. Then the cells fixed by using Karnovsky's fixative (mixed with 2 % paraformaldehyde and 2 % glutaraldehyde) for 2 h at 4°C. Samples were washed with distilled water and post-fixation was conducted by using 1 % osmium tetraoxide at 4°C for 2 h. The cells were enbloc stained with 0.5 % uranyl acetate at 4°C for 1 h and then dehydrated by ethanol. Then transition was conducted by 100 % propylene oxide at room temperature each for 10 min and infiltrated in Spurr's resin followed by 1:1 Spurr's resin: propylene oxide for 2 h. Cells were embedded in Spurr's resin and sliced by ultramicrotome. The samples were observed by TEM (JEM1010, JEOL) at 80 kV.

The viability of cells was measured by using 0.4 % of tryphan blue solution (Aldrich). This method would make dead cells distinguished from livecells. The dead cells were stained with tryphan blue and colored as dark blue. The assay was conducted in cover slip placed 12-well plates (Nunc, Thermo Fisher Scientific, USA) and the cells are seeded with 10^4 cells per well and incubated for 24 h. Then, cells were treated with different concentration of GO-HNP-PpIX (25, 50, 75, and 100 μg mL^{-1}). Then, the culture medium was removed and cells were washed with 0.1 M Hank's balanced salt solution (HBSS) to remove unbound nanoparticles. Subsequently, cells were irradiated with 0.8 W cm^{-2} of NIR laser (5 min) and visible light in a different time scale (0, 5, 10, and 15 min). For control experiment, both cell lines were incubated with different particles (GO-HNP and HNP-PpIX were treated at the equivalent 10 μg mL^{-1} of HNPs concentration; 10 μg mL^{-1} of HNPs is a drug carrier concentration in a 100 μg $mL^{-1}$of GO-HNP-PpIX concentration). Cell viability was determined as the percentage of the livecells over the overall cell count of the control experiment.

The MCF-7 was cultured at a density of 3 x10^4 cells per well in cover slip placed 12-well plates (Nunc, Thermo Fisher Scientific, USA) and incubated for 24 h. Then, cells were treated with HNP-PpIX, and GO-

HNP-PpIX (100 μg mL^{-1}) for 24 h. After nanoparticle incubation, the plates were washed with 0.1 M PBS for 3 times. Subsequently, the cells were irradiated with different time scale (0, 5, 10, and 15 min). Complete the irradiation step, DeadEnd™ Fluorometric TdT-mediated dUTP Nick-End Labeling (DeadEnd™ Fluorometric TUNEL assay; Promega, USA) and Fluoroshield™ with 4′,6-Diamidino-2-phenylindole dihydrochloride (Fluoroshield™ with DAPI; Aldrich) staining was carried out. Livecell fluorescent images were obtained by using a Super-resolution confocal microscope SP8 X (Leica, Germany). The dead cells were distinguished by using a fluorescence microscope with appropriate filters. The dead cells exhibited bright green fluorescence at 488 nm, while viable cells emitted weak fluorescence.

Reactive oxygen species (ROS) generation in cells was observed by Rhodamine-123 (Rh-123; Invitrogen, Grand Island, NY) staining followed by flow cytometric measurement of the fluorescence. Rh-123 is a specific dye that can directly act on mitochondria. Cells were incubated in sterile culture dishes (Nunc, Thermo Fisher Scientific, USA) at a density of 5×10^5 per dish and incubated for 24 h. Then, cells were treated with GO-HNP-PpIX (25, 50, 75, and 100 μg mL^{-1}) for 24 h. After washing with 0.1 M PBS, cells were suspended in 0.1 M HBSS, stained

with Rh-123, and analyzed by flow cytometry (FACs Calibur, BD Bioscience, USA).

2.2 Alkaline earth metal ion-doped hollow nanoparticles for neuron development

2.2.1 Fabrication of Alkaline earth metal ion-doped hollow nanoparticles

Monodisperse SiO_2 NPs were prepared by the Stöber method. Briefly, 3 mL of tetraethyl orthosilicate (TEOS) was added to a mixture of ethanol (74 mL) and ammonia (3 mL), and reacted for 6 h at 40°C. Then, titanium (IV) isopropoxide (TTIP; 3.6 mL), ethanol (18 mL), and acetonitrile (6 mL) were introduced in SiO_2 solution forthe titania-coated layer. The mixture solution was stirred for 6 h at 5°C. To fabricate HNPs (p-HNP, Mg-HNP, Ca-HNP, Sr-HNP, and Ba-HNP), the resulting CSNPs were treated with magnesium hydroxide (0.02 M), calcium hydroxide (0.05M), strontium hydroxide (0.1 M), and barium hydroxide solution (0.2 M) under sonication for appropriate treatment time, respectively. The products were thoroughly washed with DI water and 0.1 M PBS solution. To load NGF into the HNPs, 4 μg NGF (Sigma, St. Louis, MO, USA) was added to the HNPs in DMSO (1 mg mL^{-1}). After being stirred for 24 h, NGF-loaded HNPs were collected by centrifugation and dried in vacuum oven at 20°C for 48 h to remove

DMSO. The dried NGF-encapsulated HNPs were washed with 0.1 M PBS to remove absorbed NGF on the surface of the HNPs.

2.2.2 Characterization of Alkaline earth metal ion-doped hollow nanoparticles

TEM images were acquired with a JEM-200CX (JEOL). Atomic percent of the elements (Si, Ti, Mg, Ca, Sr, and Ba) were calculated by FE-SEM (JSM-6701F, JEOL) equipped with an EDS facility (INCA Energy). The XPS spectra were obtained with an AXIS-His (KRATOS).

2.2.3 Application for Neuron development promoter

Rat pheochromocytoma PC-12 cell were purchased from ATCC (American Type Culture Collection, Manassas, VA, USA). For differentiation of PC12 cells, cells were seeded and incubated for 24 h in a serum-reduced medium before treatment with the HNPs. The HNPs were inserted into the medium at concentrations ranging from 5 to 25 μg mL^{-1}. Simultaneously, 100 ng mL^{-1} of NGF and 0.1 % bovine serum albumin (BSA) were added into the medium to induce the differentiation of PC-12 cells. Fresh NGF and BSA were supplied to the medium every day. The β-tubulin (III) expression is evidence for differentiation of PC-12 cells. The cells were immunostained with Alexa Fluoro 488 mouse anti-β-tubulin, Class III (neuron specifi c; BD bioscience, San Jose, CA, USA) for overnight at 37°C. After being washed with 0.1 M PBS, the samples were mounted using Fluoroshield with DAPI (4,6-diamidino-2-phenylindole dihydrochloride; Sigma, USA) and observed by Delta Vision RT imaging system (Applied Precision, Issaquah, WA). The images were taken by Cascade II electronmultiplying charge-coupled device (EMCCD) camera.

Neurite outgrowth of PC-12 cells was calculated in a treatment-time

dependent manner.

Based on the immunofluorescent images, differentiation efficiency and average neurite length were calculated using ImageJ software (NIH, Bethesda, MD, USA). Neurite-bearing cells were defined as cells with at least one neurite longer than the cell body diameter. The differentiation efficiency was assessed by dividing the number of neurite-bearing cells by the total number of cells. The neurite length was defined as the distance from the cell body to the end of the neurite. In case of branched neurites, the length of the longest branch was measured, and then each branch was estimated from the end of the neurite to the neurite branch point. Average neurite length was calculated by dividing the sum of neurite length by the number of neurite. Independent experiments were performed three times and neurite-bearing cells and average neurite length were analyzed randomly selected three different images for each condition (n = 9). More than 100 cells were counted in each condition.

2.3 GQD/PPy coated hollow nanoparticles for bioimaging and drug delivery

2.3.1 Fabrication of GQD/PPy coated hollow nanoparticles

In the synthesis of silica/titania hollow nanoparticles (HNPs), a colloidal solution of SiO_2 was prepared by using the Stöber method. Tetraethyl orthosilicate (3 mL) was added to a mixture of ethanol (74 mL) and ammonia (3 mL). The mixture was stirred for 6 h at 40°C. Next, a mixture of titanium (IV) isopropoxide (TTIP; 3.6 mL), ethanol (18 mL), and acetonitrile (6 mL) was added to the colloidal SiO_2 solution and stirred at 5°C for 6 h. The resulting SiO_2/TiO_2 core/shell nanoparticles were then treated with ammonia hydroxide solution (15 mL) for 24 h. Simultaneously, redeposition of etched silica occurred under basic conditions to give HNPs comprised of silica and titania. After the reaction, the synthesized HNPs were isolated from solution by centrifugation (Mega 17R, Hanil Science and Industrial) and redispersed in water (50 mL). For polypyrrole surface coating, $FeCl_3$ was treated with HNPs. 1.5 g of $FeCl_3$ and 0.5 g of HNPs was mixed in 100 mL of distilled water for introduce oxidant to the surface of the HNPs. The

HNPs were then centrifuged and resuspended with normal hexane solution. Subsequently, 1 mL of pyrrole monomer was dropped into the above mentioned solution. Furthermore, to introduce graphene quantum (GQD) dot to the surface of HNPs, the GQD solution was added with the pyrrole monomer to the $FeCl_3$ treated HNPs.

.

2.3.2 Characterization of GO wrapped hollow nanoparticles

Transmission electron microscopy (TEM) images of HNPs were obtained by using a JEOL EM-2000 EX II microscopy, and the size distribution and zeta potential of HNPs were measured by using ELS-8000 instrument (Otsuka Electronics, Japan). EDS analysis was carried out by using a JEOL JSM-6700 F microscope with an EDS facility. The BET surface area and average pore volume was analyzed by ASAP 2000 (Micromeritics, USA). Fourier transform infrared (FTIR) spectra were obtained using a FT-IR Frontier (PerkinElmer, USA) in absorption mode at a resolution of 64 cm^{-1}. Ultraviolet-visible (UV-Vis) spectra were acquired using a Lambda-20 spectrometer (PerkinElmer, USA). Photoluminescent absorption spectra were gained with LS-55 spectrofluorometer (PerkinElmer, USA).

2.3.2 Application for Bioimaging system

Human breast cancer MCF-7 cells were purchased from American Type Culture Collection (Manassas, VA, USA). Both cells were cultured in RPMI-1640 medium with 10 % fetal bovine serum and 1 % penicillin-streptomycin solution. They were maintained in a 75T flask at 37°C in humidified 5 % CO_2 atmosphere and passaged at 70-80 % confluence. MCF-7 cells were spread at a density of 3000 cells per well, in 8-well Lab-Tek II chambered coverglass (Nunc, Thermo Fisher Scientific, USA) and treated with 25 μg mL^{-1} of GQD/PPy-HNP. After 24 h, the supernatant was removed and the cells were washed twice with 0.1 M phosphate buffered solution (PBS). The cells were analyzed with a Delta Vision RT imaging system (Applied Precision, Issaquah, WA, USA) under 5 % CO_2 at 37°C. To obtain images, a Cascade II electron multiplying charge-coupled device camera was used. The excitation and emission filter were used as FITC, to restriction of the fluorescence lamp of the instruments.

2.3.4 Application for Stimuli-responsive drug release

Dexamethasone (DEX) was utilized as the model drug for electrical stimuli responsive drug release systm. The stimuli responsive release study was performed. The platinum anode and silver chloride (Ag/AgCl) cathode was immersed in phosphate buffered saline (PBS, pH 7.2) with a separated distance of 1 cm^{-1}. The GQD/PPy-HNP and PPy-HNP nanoparticles in the solified gel was calculated to be 1 wt %. For the relase study in solution, specific voltages were applied between the two electrodes, followed by measurements of the concentration of released molecules by UV-Visible spectroscopy.

For observe in vitro study of the released drug, the cells were plated at a density of 5000 cells per well in 8-well Lab-Tek II chambered cover glass (Nunc, Thermo Fisher Scientific, USA) and treated with DEX solution released from GQD/PPy-HNP for 24 h. After treatment, propidium iodide (PI; Vybrant apoptosis kit, Molecular Probes, Invitrogen, Grand Island, NY) staining was carried out. Livecell fluorescent images were obtained by using a Delta Vision RT imaging system (Applied Precision, Issaquah, WA) and Cascade II electron-multiplying charge-coupled device (EMCCD) camera. Dead cells were

distinguished by using a fluorescence microscope with appropriate filters. The PI was excited by a wavelength of 535 nm. Viable cells do not exhibit any fluorescence due to the impermeability of dye, while dead cells emit red fluorescence.

3. Results and Discussions

3.1. GO wrapped hollow nanomaterials for phototherapy

3.1.1 Fabrication of GO wrapped hollow Nanoparticles

The synthesis of GO–HNP–PpIX was shown in **Figure 15**. Silica nanoparticles were fabricated by the Stöber method [36]. By adding titanium tetraisopropoxide (TTIP) to the silica nanoparticles, titania layers were introduced onto the surface of the silica nanoparticles. The HNPs were made by adding these silica/titania core/shell nanoparticles (CSNPs) to aqueous ammonium hydroxide (NH_4OH), which dissolved the silica core and redeposited silica on the surface of the titania shells [37]. The HNPs and protoporphyrin IX (PpIX) were then mixed in dimethyl sulfoxide (DMSO) and stirred for 24 h to encapsulate the PpIX within the HNPs (HNP–PpIX). After loading the PpIX into the HNPs, the surface of the HNPs was pre-modified with (3-Aminopropyl-triethoxysilane (APTES; APTES–HNP–PpIX) and then post-modified with GO (GO–HNP–PpIX). Transmission electron microscopy (TEM) images and electrophoretic light scattering (ELS) data confirmed that the HNPs had an average diameter of 46.3 nm with a narrow size distribution

(**Figure 16a**). After GO treatment, the diameter of the HNPs increased by 14 nm, while the dispersity and uniformity in size and shape were unchanged (**Figure 16b**). Further, the fabricated graphene oxide (GO) with *ca.* 200 nm size was confirmed by atomic force microscope (AFM) **(Figure 17a)**. By calculating the surface area of the HNPs, it would be concluded that 200 nm sized GO was appropriate for wrapping HNPs without aggregation and multiple enwrapment of HNPs. Fourier transform infrared spectroscopy (FT-IR) confirmed the each synthesis process (**Figure 17b**). The spectrum of the HNPs had characteristic peaks at 784, 948, 1070, and 1402 cm^{-1} corresponding to Si-O stretching, Si–O–Ti vibrations, Si–O stretching, and Si–O stretching overtone vibrations, respectively [38-40]. GO-HNP had a CH_2 deformation at 745 cm^{-1}, a Si-CH=CH_2 in plane deformation peak at 1385 cm^{-1}, and a C=C stretching vibration at 1610 cm^{-1}, indicating the enwrapment of GO of HNP's surface [40-43]. The increased intensities of the C–N stretching band at 1076 cm^{-1} and the C=O stretching band at 1724 cm^{-1} confirmed the surface treatment with GO [40, 44]. The characteristic peaks of GO–HNP–PpIX at 1261 cm^{-1} (aromatic C–H vibration) and 698 cm^{-1} (CH_2 rocking vibration of Si–CH_2–R) demonstrated the successful surface functionalization of GO [45, 46]. The peak assignments were

summarized in **Table 1**.

The UV/vis absorption spectra of HNP-PpIX and GO–HNP–PpIX dispersed in DMSO are shown in **Figure 17c**. In DMSO, PpIX loaded in HNP–PpIX dissolved as a monomer with a sharp Soret band at 402 nm. The PpIX was present as aggregates in GO-HNP-PpIX; a broadened split Soret band of moderate intensity was observed, suggesting a successful surface encappment of HNP by GO wrapping [47]. **Figure 17c** exhibits that PpIX fluoresces strongly at 632 nm (λ_{ex}: 402 nm) in DMSO. While, the aggregated PpIX in the interior of GO-HNP had a diminished fluorescence with a blue shift of the emission peak to 620 nm (λ_{ex}: 402 nm). PpIX completely dissolved in DMSO and exited the HNPs. In case of GO-HNP-PpIX, the PpIX was not soluble in GO-HNPs and remained aggregated inside the HNPs because of a GO induced surface capping.

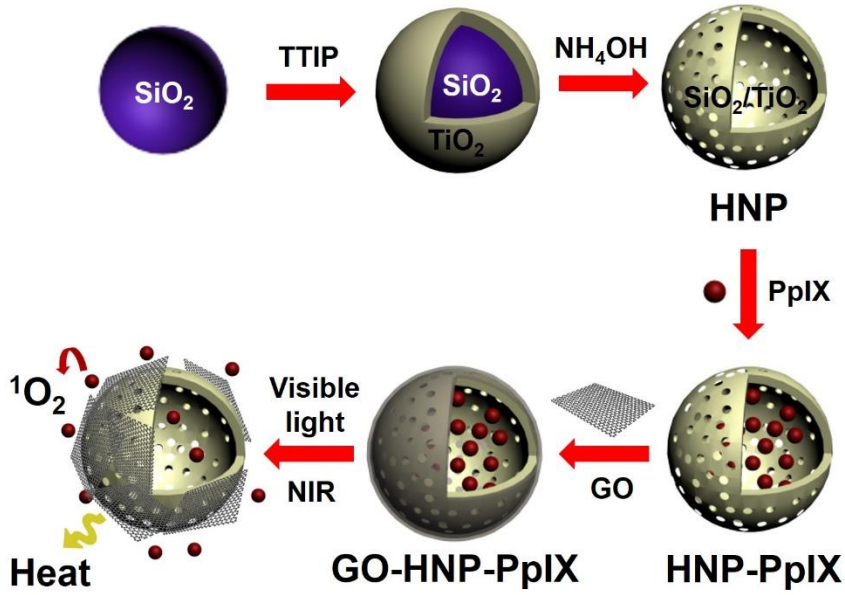

Figure 15. Schematic illustration of fabrication of GO-HNP-PpIX. GO-HNP was used as encapsulating agent for PpIX. The fabricated GO-HNP-PpIX exhibited light responsive singlet oxygen and heat generation properties.

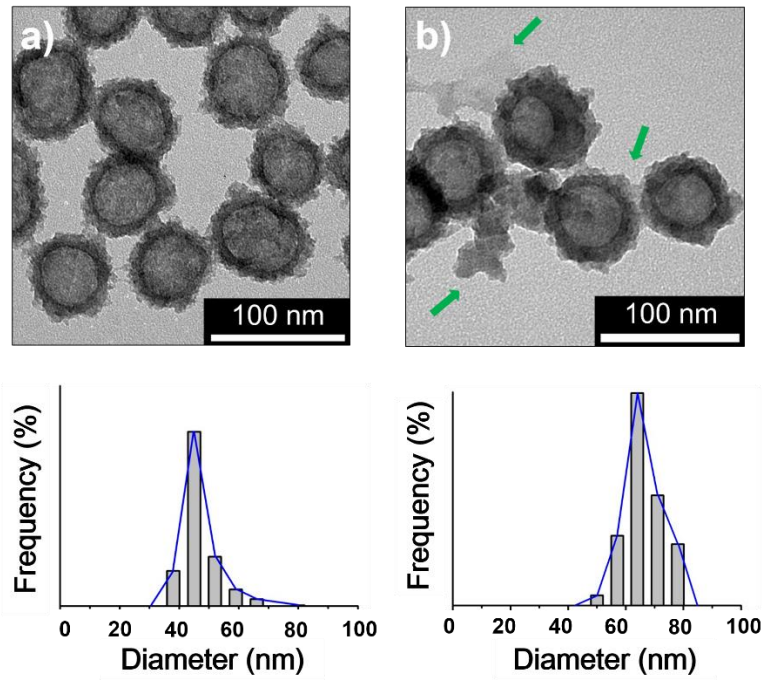

Figure 16. TEM images of a) HNP and b) GO-HNP-PpIX (below: size distribution histograms determined by ELS). Green arrow indicates GO enwrapment of HNPs.

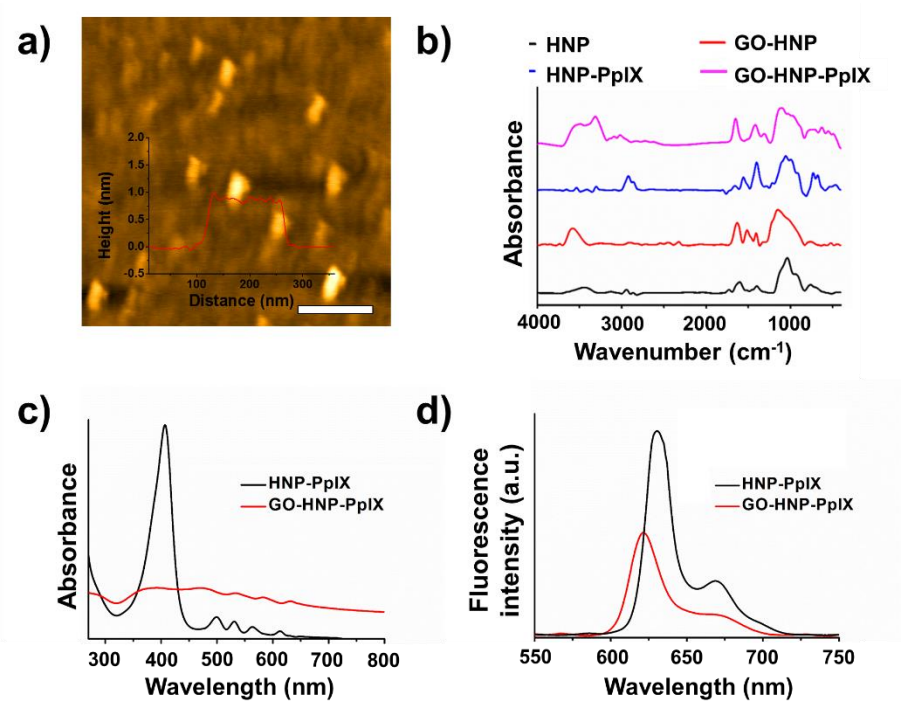

Figure 17. a) AFM image of 200 nm graphene oxide (scale bar: 500 nm). b) Infrared spectroscopy absorbance spectra of HNPs, GO-HNP, HNP-PpIX, and GO-HNP-PpIX. c) UV-visible spectroscopy absorption spectrum and d) Fluorescence intensity of HNP-PpIX and GO-HNP-PpIX in DMSO.

Table 1. Peak assignment of HNP, GO-HNP, HNP-PpIX, and GO-HNP-PpIX.

Materials	Wavenumber (cm^{-1})	Assignments
HNP	1402	Si-O overtone
	1070	Si-O stretching
	948	Si-O-Ti
	784	Si-O stretching
GO-HNP	3400	-OH stretching
	1630	C=C stretching
	1385	Si-CH=CH_2 in-plane deformation
	745	CH deformation of C-O
HNP-PpIX	1730	C=O stretching
	1596	Pyrroline C=N stretching
	1084	C-N stretching
	812	Si-CH_3 rocking vibration
GO-HNP-PpIX	2949	C=C symmetric deformation
	1260	C-H vibration
	690	Si-CH_2-R vibration

Figure 18 shows the nitrogen adsorption isotherm and the average pore volume of the HNPs. They had a Brunauer-Emmett-Teller (BET) surface area of 313 m^2 g^{-1}. The Barret, Joyner and Halenda (BJH) pore size distribution of HNPs were exhibited in **Figure 18 c** (shell pore: 2 nm, cavity pore: 30 nm). The large hollow cavities and the mesoporous shells of HNPs suggested a therapeutic application for delivering drugs [48, 49]. After wrapping the GO onto the surface of the HNPs, the surface area of nanoparticles were exhibited as 28.02 m^2 g^{-1}. Furthermore, the pore size distribution of GO-HNPs were evaluated (Figure 18 d), which BJH data exhibiting the complete 2nm shell pore blocking and non-blocking of 30 nm cavity pore. By this result, the loaded drug would be remained inside of the HNPs cavity, when GO wrapping was maintained on the surface of the HNP's surface.

To investigate the drug loading possibility, the loading capacity was evaluated by ultraviolet/visible (UV/vis) spectroscopy [50]. The loading capacity of the HNPs (1.645 μmol of PpIX were loaded into 1 mg of HNP–PpIX) is about 40 times higher than that of previous mesoporous silica nanoparticles [51].

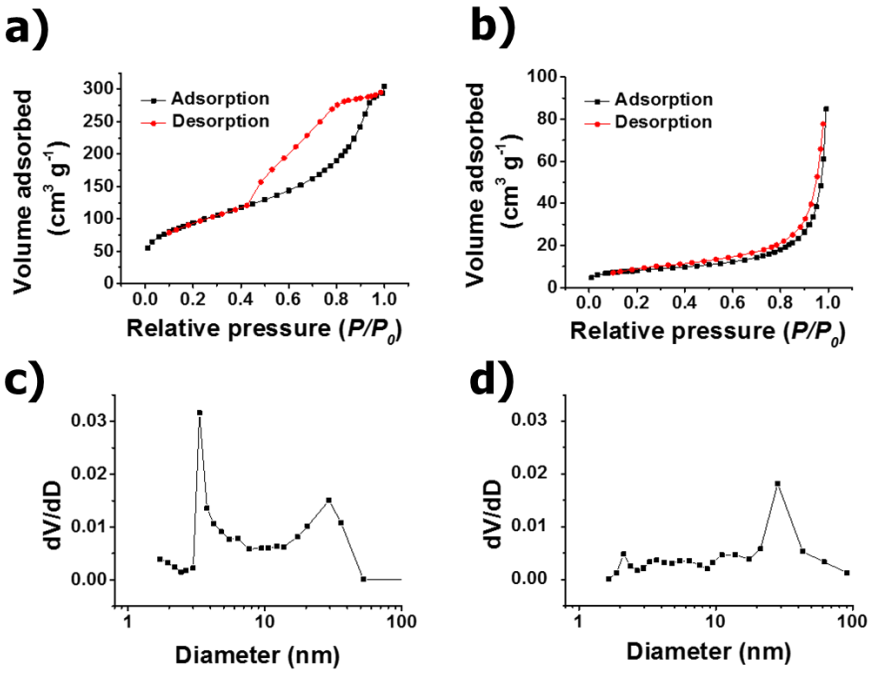

Figure 18 Nitrogen adsorption isotherm of the a) HNPs (BET surface area 310.5593 m^2 g^{-1}) and b) GO-HNPs (BET surface area : 28.0236 m^2 g^{-1}. The nitrogen adsorption isotherm demonstrates the pore size distribution of c) HNPs (cavity size: 32 nm, inter-shell pore: 1.8 nm) and d) GO-HNPs (cavity size: 27 nm, inter-shell pore: 1.1 nm).

GO absorbs an NIR and exhibits heating property which makes GO a useful phtothermal therapy (PTT) agent. The heat generation upon NIR irradiation was calculated to demonstrate thermal energy conversion from NIR laser. The HNP-PpIX and GO-HNP-PpIX was dispersed in distilled water and irradiated for 15 min. As shown in **Figure 19a**, the HNP-PpIX solution exhibited no response to NIR irradiation, whereas GO containing solution demonstrated significant dose dependent heat generation under NIR irradiation condition.

The drug release of HNP-PpIX and GO-HNP-PpIX was evaluated by UV/Vis spectroscopy. The nanoparticles was dispersed in DMSO (an intracellular environment) and sonicated for 360 min (**Figure 19b**). To determine the NIR laser induced PpIX release property, the GO-HNP-PpIX solution was irradiated with NIR for 15 min. The drug release profile exhibited that GO-HNP-PpIX response under NIR irradiation and release PpIX efficiently (*ca.* 82 %). However, the GO–HNP–PpIX released very little PpIX even after 360 min in dark condition mainly because of a few leakage of PpIX. The result indicated that fabricated GO-HNP-PpIX had stimuli responsive drug release property upon NIR irradiation. In addition, GO–HNP could load a large amount of PpIX and

deliver the PpIX effectively to the inner phase of cancer cells without leakage.

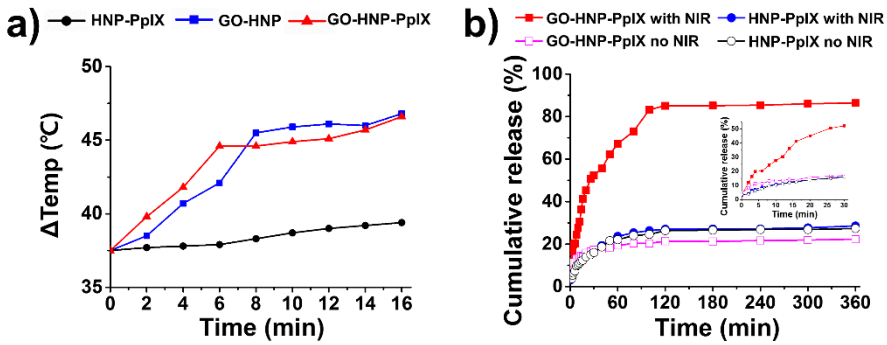

Figure 19. a) Heating curves of HNP-PpIX, GO-HNP, and GO-HNP-PpIX (1 mg mL^{-1}, 3mL) under 808 nm laser irradiation at a power density of 0.8 W cm^{-2}. b) Time dependent cumulative PpIX drug release profile of GO-HNP-PpIX and HNP-PpIX (0.5 mg mL^{-1}, 3 mL) in a condition of with or without NIR irradiation.

The $^1O_2$ generation efficiency of photosensitizers is an important factor in PDT [52]. As light sources the NIR laser and LED light was used for this study because of its tissue penetration property and safety toward the cells. To confirm the photodynamic activity of the GO–HNP–PpIX, $^1O_2$ generation was detected by a chemical trapping method using 9,10-anthracenediyl-bis(methylene)dimalonic acid (ABDA) [53]. ABDA reacts with the generated $^1O_2$ and causes a decrease in the ABDA absorption peak at 380 nm [54, 55]. To monitor the amount of $^1O_2$ generation from the GO–HNP–PpIX as a function of the irradiation time, the ABDA was dropped into GO–HNP–PpIX and irradiated for different times at intervals of 3 min; control samples were placed in a dark room. **Figure 20** and **Figure 21** shows how the absorbance spectra of ABDA decreased in solutions containing GO–HNP–PpIX. The time-dependent ABDA consumption was observed under irradiated and non-irradiated conditions. The absorption of the irradiated sample decreased, while no significant changes were observed in non-irradiated samples. At 10 min, there was a noticeable difference in absorbance between the irradiated and non-irradiated samples. This finding suggested that PDT would be helpful only after 10 min of irradiation. The $^1O_2$ generation from

irradiated GO–HNP–PpIX indicates this system is suitable for destroying cancer cells *via* PDT.

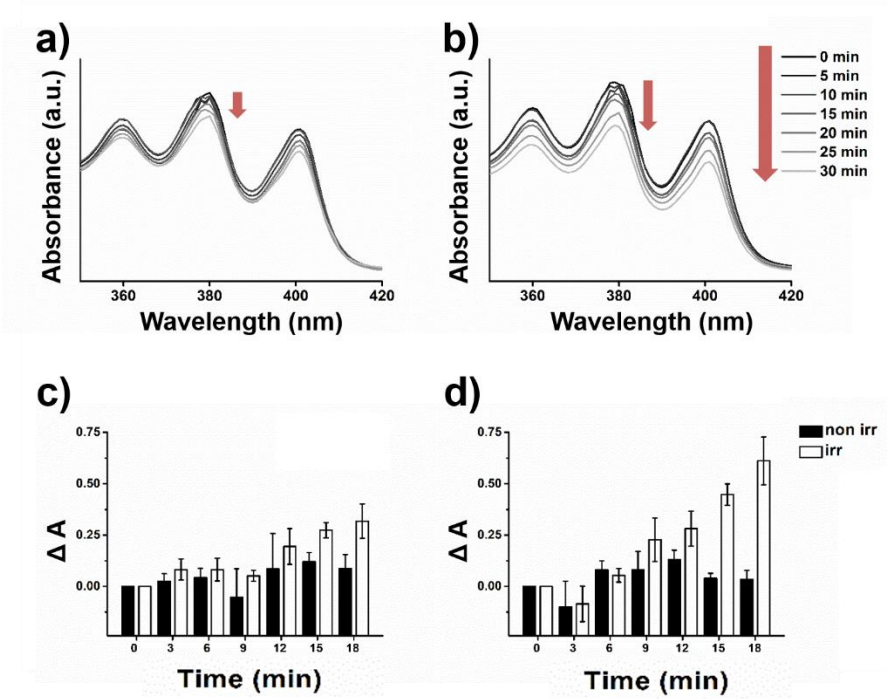

Figure 20. Photobleaching of ABDA (0.07 mg mL^{-1}, 3 mL) by GO-HNP-PpIX (0.3 mg mL^{-1}) nanoparticles dispersed in 0.1 M PBS. Absorbance spectra of GO-HNP-PpIX nanoparticles in a condition of a) without NIR laser irradiation and b) with NIR laser irradiation were observed with different time scale by using visible light. Below: the change of absorption intensity of ABDA without light and irradiated GO-HNP-PpIX nanoparticles. (black: with irradiation, white: without irradiation). Values exhibit mean ± SD, and each experiment was performed in triplicate.

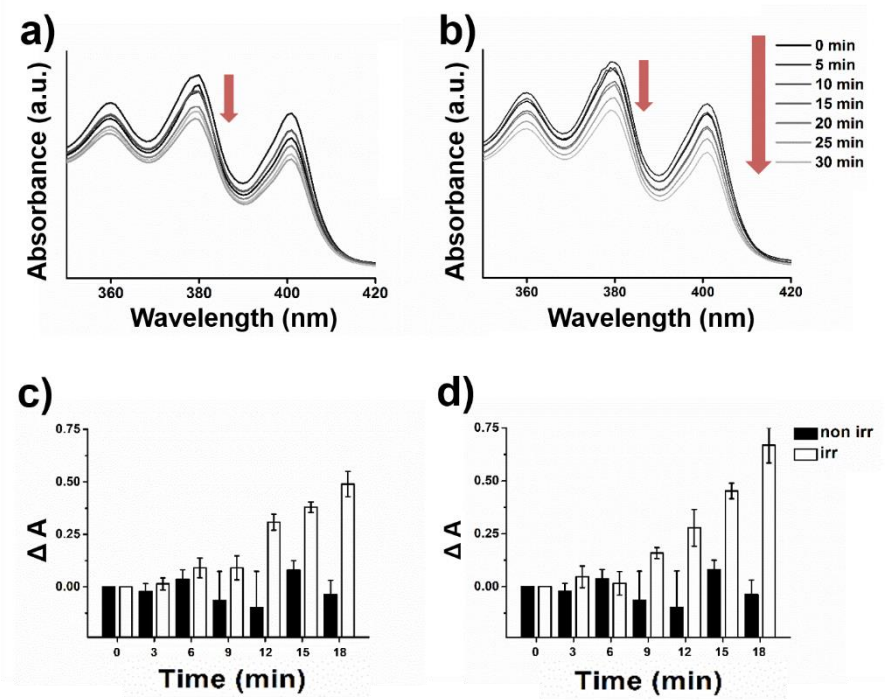

Figure 21. Photobleaching of ABDA (0.07 mg mL^{-1}, 3 mL) by HNP-PpIX (0.3 mg mL^{-1}) nanoparticles dispersed in 0.1 M PBS. Absorbance spectra of HNP-PpIX nanoparticles in a condition of a) without 808 nm laser irradiation and b) with 808 nm laser irradiation were observed with different time scale by using visible light. Below: the change of absorption intensity of ABDA without light and irradiated GO-HNP-PpIX nanoparticles. (black: with irradiation, white: without irradiation). Values exhibit mean ± SD, and each experiment was performed in triplicate.

3.1.2. Application for phototherapy

Cellular distribution of GO-HNP, HNP-PpIX, and GO-HNP-PpIX was observed by TEM (**Figure 22**). MCF-7 human breast cancer cells were used to investigate the effects of nanoparticles. TEM images showed that particles were taken up into the cells by an endocytic-pathways. The intracellular particles remained their original spherical hollow shape, and most of the HNPs were located in the endosome/lysosome. Furthermore, the HNPs were evenly distributed throughout inner cell cytoplasm. In addition, the cellular structures were not damaged, which result suggesting that the internalized HNPs did not induce cell damage to the cells. However, at some level, the GO-HNP-PpIX had a PTT effect in a condition of NIR irradiation. In this experiment, the PTT effect of the GO-HNP-PpIX in a condition of with or without NIR irradiation was examined. **Figure 22** and **Figure 23** exhibits that some mitochondrias were damaged and endoplasmic reticulum were disappeared or ruptured after NIR irradiation. These findings demonstrate that GO-HNP-PpIX would induce inner cell damage by GO induced PTT effect.

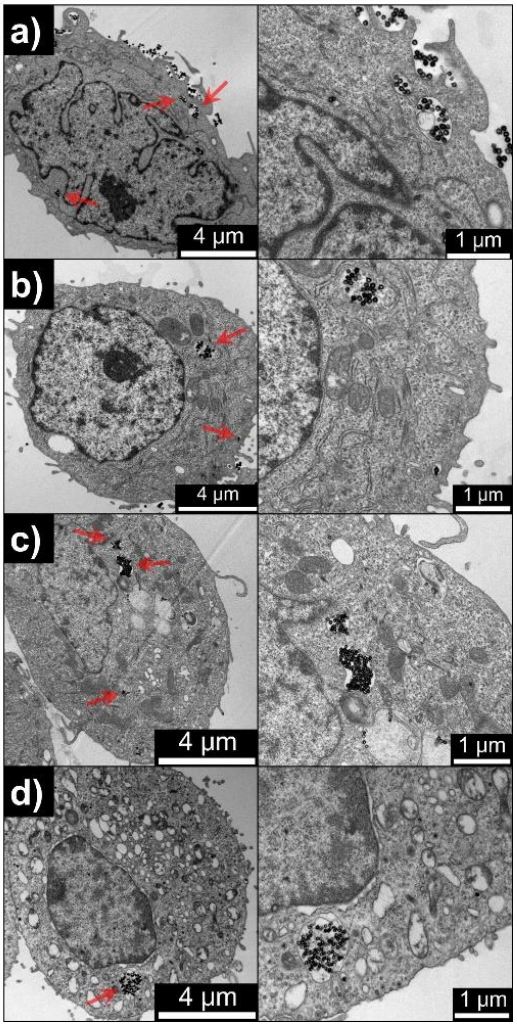

Figure 22. TEM images of particle-internalized MCF-7 cells incubated with a) HNPs, b) GO-HNP, c) GO-HNP-PpIX without NIR irradiation, and d) GO-HNP-PpIX with 0.8 W cm^{-2} of NIR irradiation. (MCF-7 cells were incubated at the equivalent 25 μg mL^{-1} HNP concentration). Right: magnified images of a), b), c), and d). (red arrows indicate the location of HNPs, GO-HNP, and GO-HNP-PpIX).

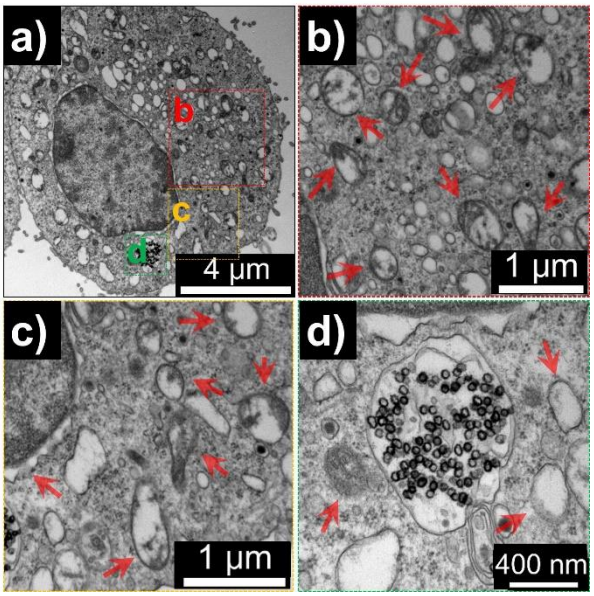

Figure 23. TEM images of GO-HNP-PpIX incubated MCF-7 cells after NIR irradiation. b), c), and d) is magnified TEM images of a). Red arrows indicate damaged cell organelles.

In this research, it is carefully designed that fabricated the GO-HNP-PpIX for multimodal therapy (**Figure 24**). Cell destruction by both PTT and PDT was studied. The cytotoxicity of HNP-PpIX and GO-HNP-PpIX to MCF-7 cells was determined by the trypan blue exclusion method. Viable cells with an intact plasma membrane are not stained, while dead cells become intensely blue [56]. MCF-7 cells were cultivated with HNP-PpIX and GO–HNP–PpIX for 24 h and further irradiated with NIR laser and LED light. In a concentration-dependent manner, without light exposure, both HNP-PpIX and GO-HNP-PpIX showed negligible dark toxicity to MCF-7 cells (**Figure 25** and **Figure 26**). In **Figure 20**, the heat generation was observed in GO contained solution, which indicates the potentials of GO-HNP-PpIX as a PTT agent. As for testing the PTT effect of GO-HNP-PpIX, the cells were irradiated with NIR laser for 15 min at the nanoparticle concentration from 20 to 100 $\mu g\ mL^{-1}$. The cell viability was observed as 76 %, whereas only 13 % of cell death was observed in HNP-PpIX incubated cells, showing that NIR induced photothermal effect was activated only GO-HNP-PpIX condition. Further, to determine the PDT efficacy of GO-HNP-PpIX, the cytotoxicity test upon NIR laser and LED light irradiation had been

carried out. As exhibited in **Figure 20**, the singlet oxygen generation ability was promoted by LED light. Therefore, when MCF-7 cells were exposed to LED light the cell viability was decreased upto 60 %, manifesting the singlet oxygen induced PDT effect. **Figure 25** shows that the cell viability decreased with increasing irradiation time and increasing GO–HNP–PpIX concentration, indicating that efficient anticancer treatment can be observed only under both NIR laser and LED light irradiation. For MCF-7 cells, the cell death is up to 97.5 % (at 100 μg mL^{-1} of GO–HNP–PpIX with 15 min of irradiation), which is about 40 times more efficient than in previous reports [57]. Moreover, the powerful anticancer activity of GO-HNP-PpIX has been observed, whereas less effective tumor destruction effect has been observed in a condition of HNP-PpIX for same irradiation time and nanoparticle concentration (**Figure 26**). This consequence was caused by the synergic effect of PTT and PDT of GO-HNP-PpIX. When stored in the dark, the degree of cell death was <10 %, showing that GO–HNP–PpIX had low dark toxicity to MCF-7 cells. The control experiment established that HNPs, GO-HNP, and HNP–PpIX did not induce significant cell death toward MCF-7 with 15-min irradiation (**Figure 27**). These data demonstrated that the combination of PTT and PDT effect, studied with

cell viability, showed a synergic effect which was concentration dependent.

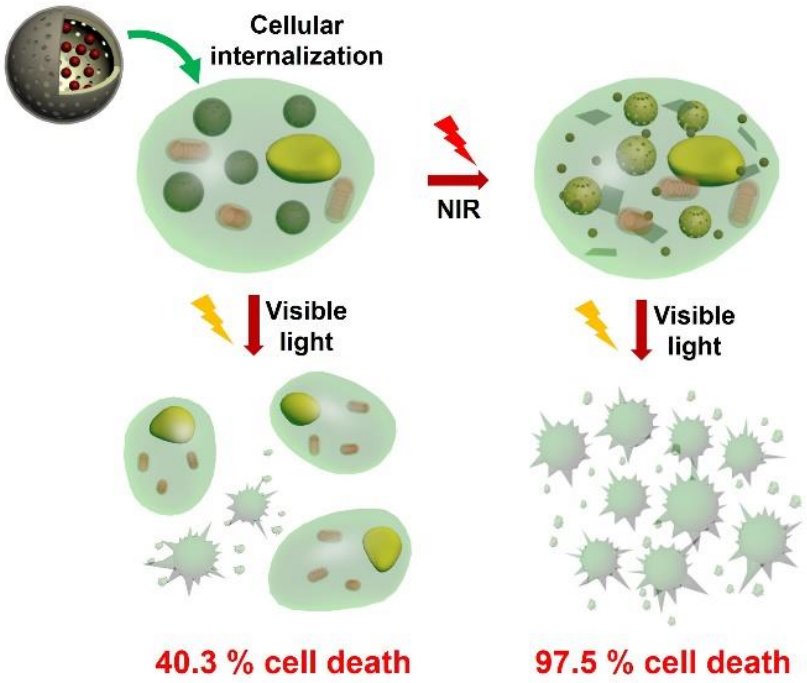

Figure 24. Shematic illustration of GO-HNP-PpIX for inducing synergic phototherapy efficacy.

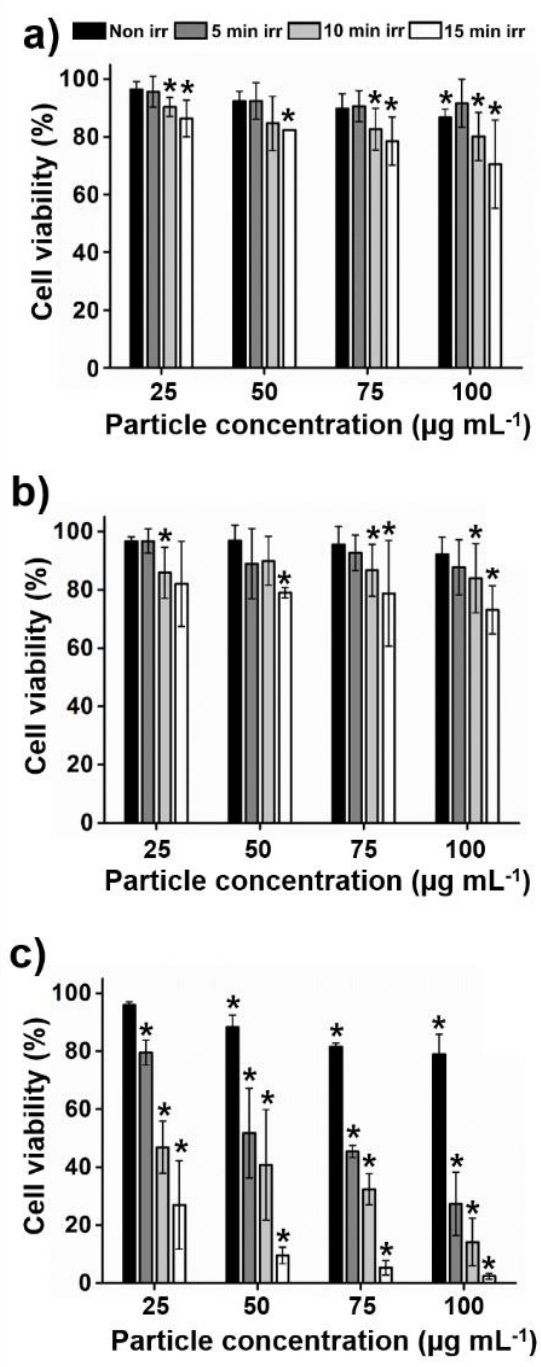
a)
Non irr
5 min irr
10 min irr
15 min irr
Cell viability (%)
Particle concentration (μg mL-1)
b)
Cell viability (%)
Particle concentration (μg mL-1)
c)
Cell viability (%)
Particle concentration (μg mL-1)

Figure 25. Cell viability of MCF-7 cells with dose (25, 50, 75, and 100 μg mL^{-1}) and irradiation time dependence (0, 5, 10, and 15 min). MCF-7 cells were incubated with GO-HNP-PpIX and irradiated with a) 0.8 W cm^{-2} of NIR laser b) visible light and c) NIR laser+visible light. Cells were irradiated after 24 h incubation of nanoparticles. Values exhibit mean ± SD and each experiment was performed in triplicate. *Statistically significant difference from negative control.

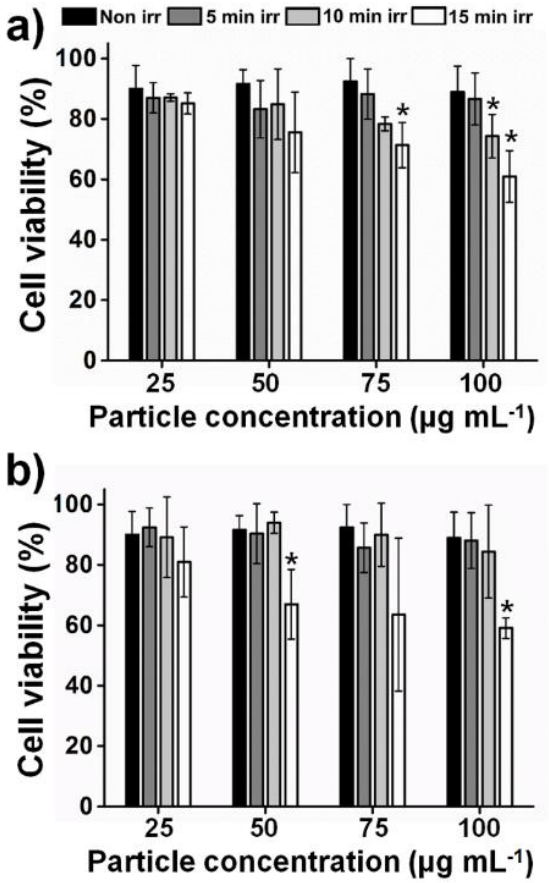

Figure 26. Cell viability of MCF-7 cells with dose (25, 50, 75, and 100 μg mL^{-1}) and irradiation time dependence (0, 5, 10, and 15 min). MCF-7 cells were incubated with a) GO-HNP and b) HNP-PpIX and irradiated with NIR laser+visible light. Cells were irradiated after 24 h incubation of nanoparticles. Values exhibit mean ± SD and each experiment was performed in triplicate. *Statistically significant difference from negative control.

3.1.7 DeadEnd™ TUNEL observation

GO–HNP–PpIX-induced phototoxicity was probated by livecell observation to investigate the PTT and PDT effect of GO–HNP–PpIX for cancer cell destruction. In this study, the cancer treatment effects were observed using MCF-7 human breast cancer cell line. The cells were incubated with different concentrations of GO–HNP–PpIX and irradiated for different times. After GO–HNP–PpIX treatment and photo-irradiation, the dead cells were stained with DeadEnd™ TUNEL system, which exhibited green fluorescence. **Figure 27** and **Figure 28** illustrates that green fluorescence was observed more with GO–HNP–PpIX incubation condition and longer irradiation time. Negligible cell death was observed under single light source systems (**Figure 28b** and **Figure 28c**). These results demonstrated that FA–HNP–PpIX had a highly active targeting ability for MCF-7 cancer cells and excellent phototherapeutic efficacy.

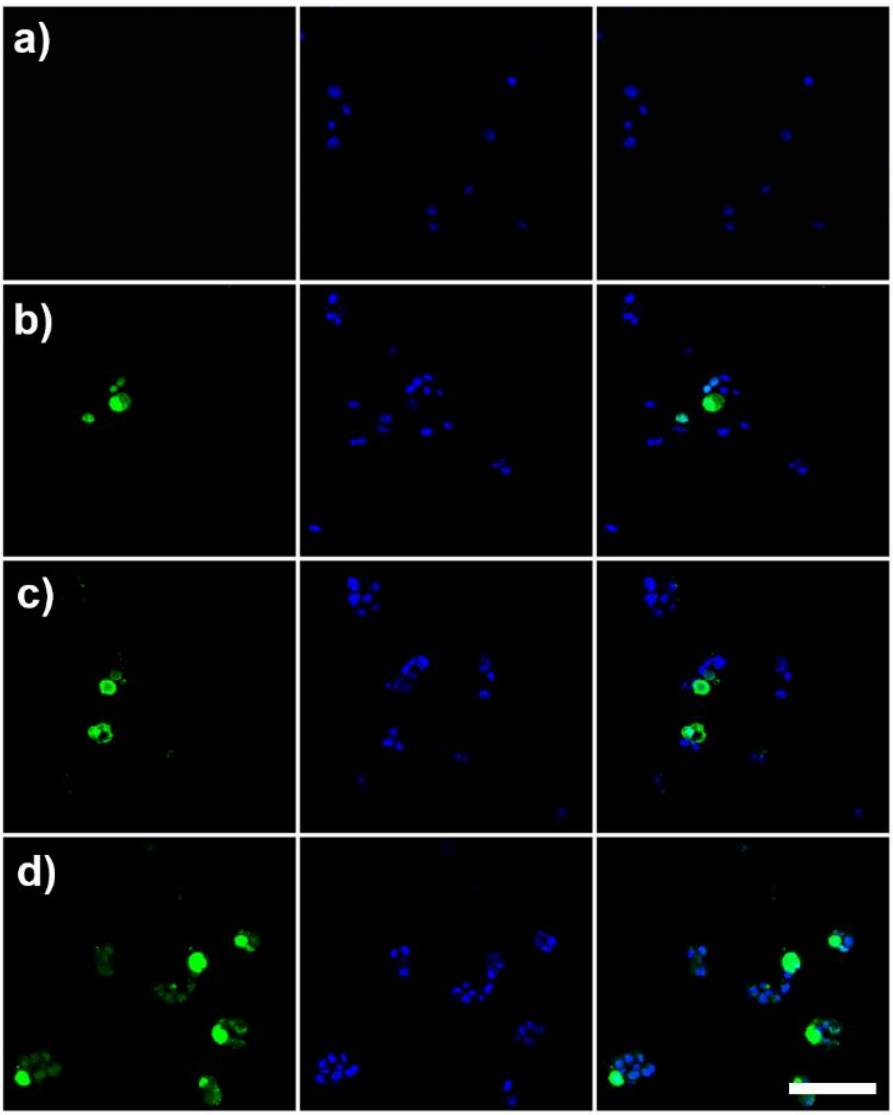

Figure 27. Livecell fluorescence images of MCF-7 cells treated with 100 µg mL^{-1} of a) no particle (control), b) GO-HNP, c) HNP-PpIX, and d) GO-HNP-PpIX. Cells were stained with DeadEnd™ Fluorometric TdT-mediated dUTP Nick-End Labeling (DeadEnd™ Fluorometric TUNEL)

assay and Fluoroshield™ with 4′,6-Diamidino-2-phenylindole dihydrochloride (Fluoroshield™ with DAPI) for visualing viable and dead cells. Each fluorescent images were taken at the same time (scale bar: 100 μm).

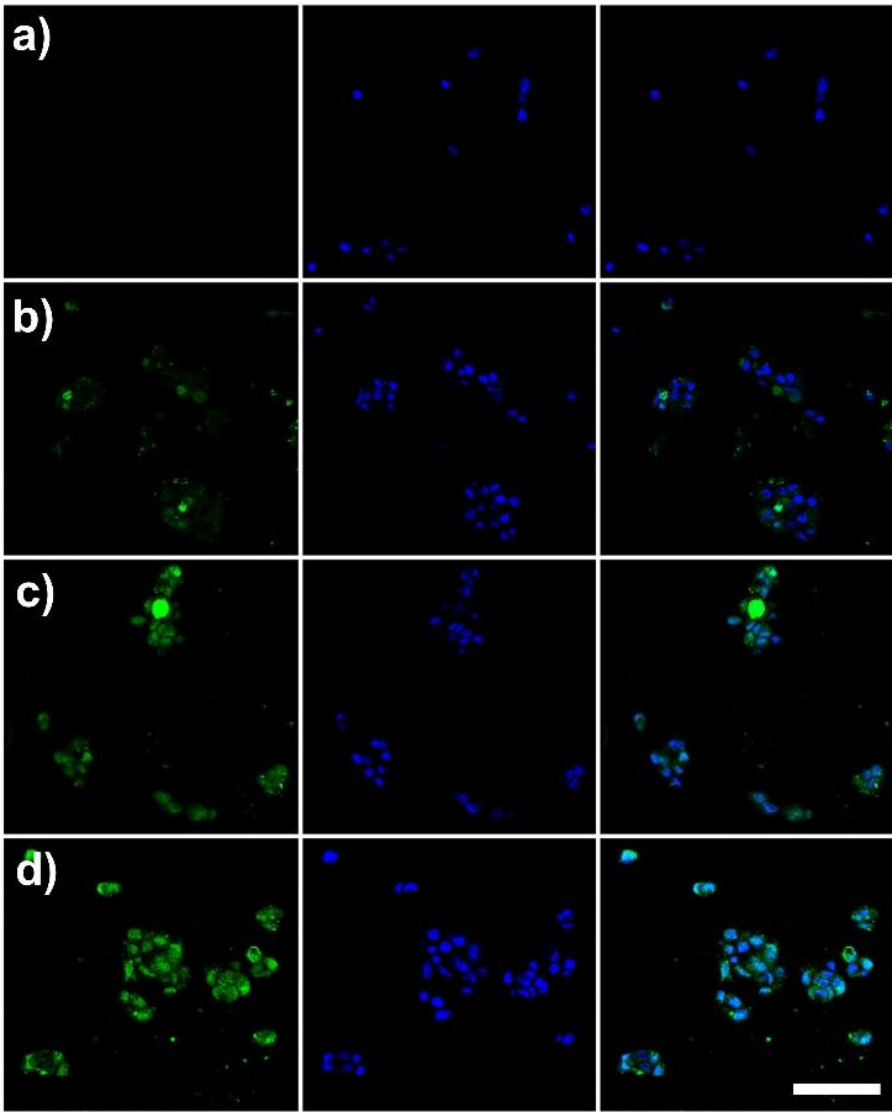

Figure 28. Livecell fluorescence images of MCF-7 cells treated with 100 μg mL^{-1} of GO-HNP-PpIX. From left to right, the visible light irradiation time is a) 0 miin, b) 5 min, c) 10 min, and d) 15 min with fixed 0.8 W cm^{-2} of NIR laser irradiation. Cells were stained with DeadEnd™

Fluorometric TdT-mediated dUTP Nick-End Labeling (DeadEnd™ Fluorometric TUNEL) assay and Fluoroshield™ with 4′,6-Diamidino-2-phenylindole dihydrochloride (Fluoroshield™ with DAPI) for visualing viable and dead cells. Each fluorescent images were taken at the same time.

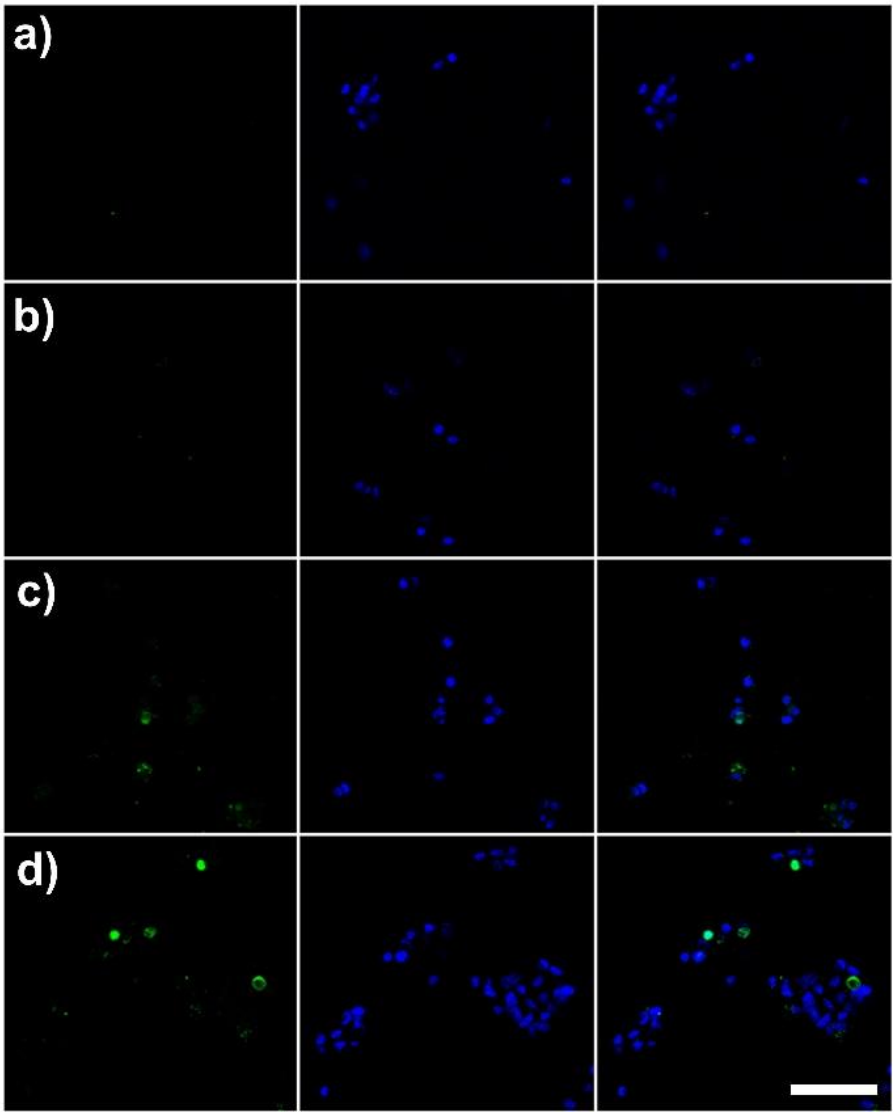

Figure 29. Livecell fluorescence images of MCF-7 cells treated with 100 μg mL^{-1} of HNP-PpIX. From left to right, the visible light irradiation time is a) 0 miin, b) 5 min, c) 10 min, and d) 15 min with 0.8 W cm^{-2} of

808 nm laser irradiation. Cells were stained with DeadEnd™ Fluorometric TdT-mediated dUTP Nick-End Labeling (DeadEnd™ Fluorometric TUNEL) assay and Fluoroshield™ with 4′,6-Diamidino-2-phenylindole dihydrochloride (Fluoroshield™ with DAPI) for visualing viable and dead cells. Each fluorescent images were taken at the same time (scale bar: 100 μm).

In this manuscript, PTT and PDT-induced total cell damage (including mitochondrial damage) was investigated by H_2DCFDA fluorescence. The H_2DCFDA dye is oxidized by intercellular ROS and emits green fluorescence. The GO–HNP–PpIX-induced cell damage was quantified by the generated H_2DCFDA fluorescence. **Figure 30a** shows that the ROS generation increased proportionally with the irradiation time (visible light). There was insignificant H_2DCFDA fluorescence change with only NIR and visible light treated samples. In this respect, GO–HNP–PpIX was ineffective under singlt light source irradiation condtion, indicating that GO-HNP-PpIX exhibited effeicient anti-cancer therapy though both NIR and visible light irradiation.

The correlation between phototoxic cell death and mitochondrial membrane potential alteration was confirmed by monitoring mitochondrial stress. Reactive oxygen species (ROS) generated by PDT can lead to the degradation of mitochondrial membrane potential integrity [41, 42]. In this regard, the mitochondrial dysfunction could be an indicator of cell damage and induce efficient cell death [58]. Mitochondrial function was investigated by monitoring changes in the intensity of Rhodamine–123 (Rh–123) fluorescence, which was used as

an indicator of membrane polarization within mitochondria [59-61]. Flow cytometry analysis was used to monitor the decrease in mitochondrial membrane potential with 100 μg mL^{-1} of GO–HNP–PpIX at different irradiation times (0, 5, 10 and 15 min) (**Figure 30b).** There were significant fluorescence intensity increases in NIR laser+visible light irradiated MCF–7 cells. However, in single light source conditions (only NIR laser or visible light), no noticeable change in fluorescence intensity was observed Depolarization of the mitochondrial membrane potential induces an increase in the Rh–123 fluorescence intensity [46, 47]. This depolarization might be followed by a cell injury step: ROS generated from PDT leads to mitochondrial membrane potential damage, resulting in mitochondrial membrane potential depolarization [48]. This result is strongly supported by the cell viability test (**Figures 25** and **Figure 26**), which is based on the high phototoxicity of GO–HNP–PpIX. Collectively, under both NIR alser and visible light irradiation, the heat and ROS generated from the GO–HNP–PpIX-induced mitochondrial depolarization and the damaged mitochondria produced mitochondrial superoxide. By these processes, the NIR and visible light source irradiated MCF–7 cells could be effectively eliminated. GO–HNP–PpIX is clearly a promising anticancer agent for tumor cells.

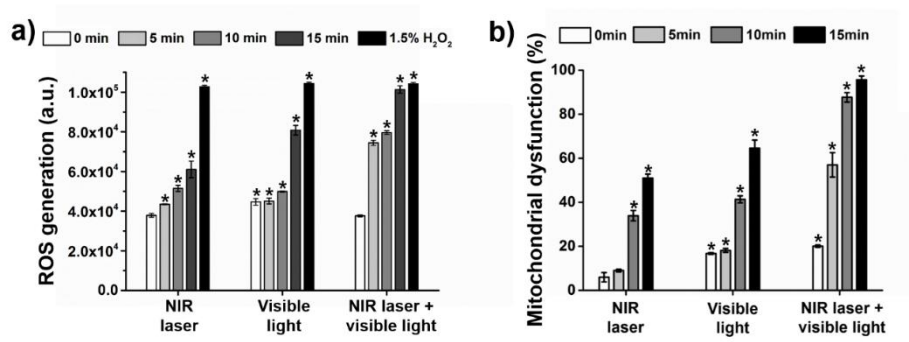

Figure 30. a) ROS generation and b) mitochondrial dysfuction of MCF-7 cells after incubation with 100 µg mL^{-1} concentration of GO-HNP-PpIX for 24 h. After incubation of GO-HNP-PpIX, cells were irradiated for different time scale 0 min, 5 min, 10 min, and 15 min (1.5 % H_2O_2 treated MCF-7 cells were used as positive control). Values exhibit mean ± SD and each experiment was performed in triplicate. *Statistically significant difference from negative control.

3.2. Alkaline earth metal ion-doped hollow nanoparticles for neuron development

3.2.1 Fabrication of Alkaline earth metal ion-doped hollow nanoparticles

Alkaline earth metal (AEM) doped SiO_2/TiO_2 hollow nanoparticles (AEM-HNPs) were fabricated by experimental procedure as indicated in **Figure 31**. SiO_2 NPs were prepared and then the titanium isopropoxide (TTIP) was added to coating the SiO_2 NPs to synthesize SiO_2/TiO_2 CSNPs. **Figure 32** shows *ca.* 40 nm of CSNP with high uniformity was successfully fabricated. After the TTIP coating procedure, the synthesized SiO_2/TiO2 CSNPs were treated with hydroxide solutions (0.02 M of $Mg(OH)_2$, 0.05 M og $Ca(OH)_2$, 0.15 M $Sr(OH)_2$, 0.1 M $Ba(OH)_2$) under sonication condition. The sonication mediated etching redeposition (SMER) method was then occurred in this process. Consequently, the hydroxide could dissolve SiO_2 core and redeposit SiO_2 to TiO_2 shell, and furthermore the AEM hydroxide was successfully doped by SMER process in a form as $M^{2+}SiO_3$ and $M^{2+}TiO_3$ (M^{2+}: divalent AEM ion) [62]. The hydroxide treatment time and concentration

is crucial for increasing the uniformity and dispersity of the divalent metal ion doped HNPs. **Figure 33** exhibits the construction changes from CSNP to HNP followed by hydroxide treatment time. As treatment time increases, the construction of CSNP became yolkshell, and hollow structure. Under insufficient treatment condition (less treatment time and hydroxide concentration), the highly mono-dispersed hollow structure did not formed and yolkshell structure has been constructed. In case of excessive hydroxide treatment condition, severely aggregated HNPs had been fabricated, which was caused by over redeposition of SiO_2 and TiO_2. Carried by several experiment, it could be concluded that 2.5 h for Ba-HNP, 2.45 h for Sr-HNP, 5 h for Ca-HNP, 16 h for Mg-HNP. This difference in treatment time was caused by the concentration of hydroxide solution, hence alkalinity (inherent solubility of AEM) [63, 64].

The HNPs had a narrow size distribution, largely in the range of 40-50 nm as determined by transmission electron microscope (TEM) images (**Figure 32**). The increment in diameter was caused by the SiO_2 core redeposion process. **Figure 34** shows the result that after determinate the hollow structure had been successfully prepared, and analyzed atomic ratio of the HNPs by Energy dispersive spectrometry (EDS). **Table 2**

demonstreated the atomic ratio of Mg-HNP, Ca-HNP, Sr-HNP, and Ba-HNP were 33:47:20 for Si:Ti:Mg, 35:45:20 for Si:Ti:Ca, 34:45:21 for Si:Ti:Sr, 35:44:21 for Si:Ti:Ba, respectively. By these TEM ans EDS results, demonstrating a large amount of Mg, Ca, Sr, Ba was successufully doped into Mg-HNP, Ca-HNP, Sr-HNP, and Ba-HNPs, respectively [65-68].

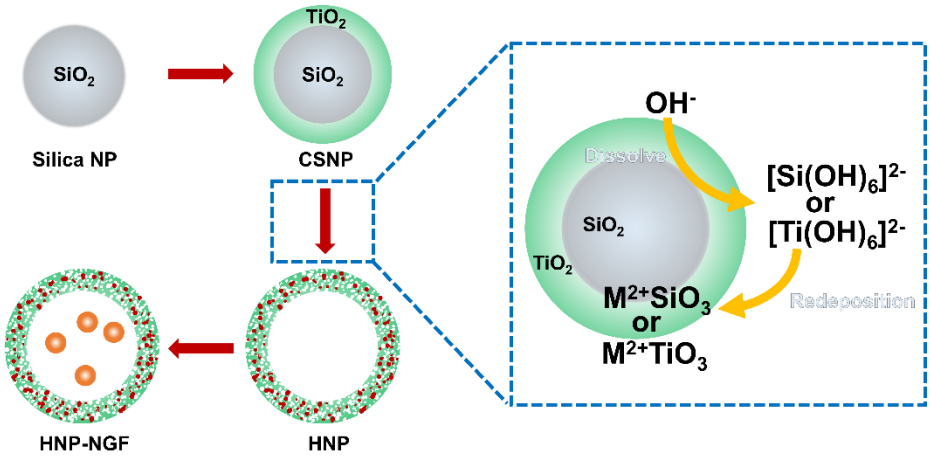

Figure 31. Illustrative diagram of the sequential fabrication procedure for alkaline earth metal ion-doped HNPs loading nerve growth factor (NGF).

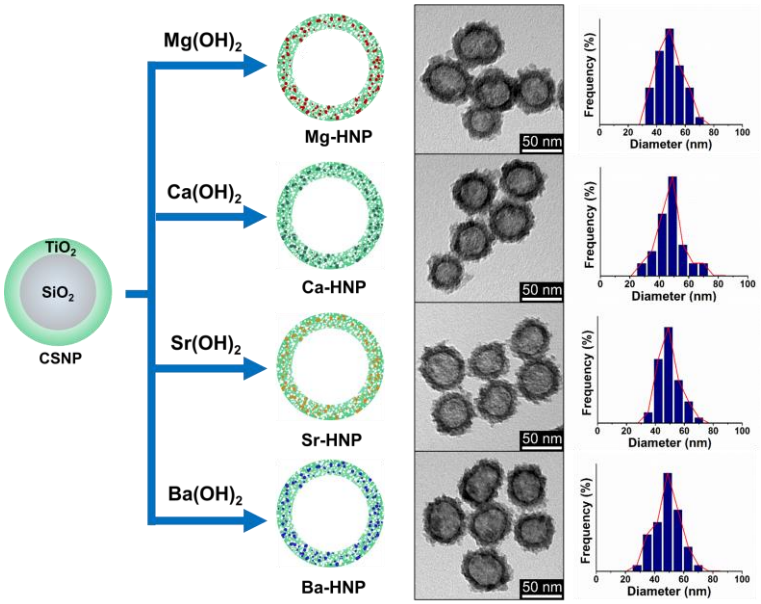

Figure 32. TEM and size distribution of HNPs.

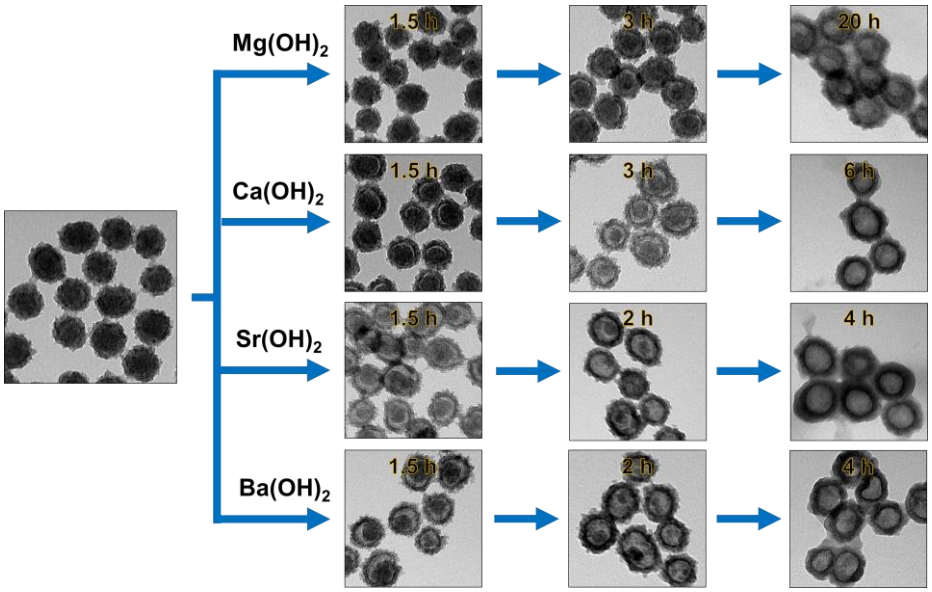

Figure 33. Doping and etching of Mg-HNP, Ca-HNP, Sr-HNP, and Ba-HNPs as a function of treatment time. Under sonication, alkaline earth metal hydroxide etched silica core as well as deposited on the shell.

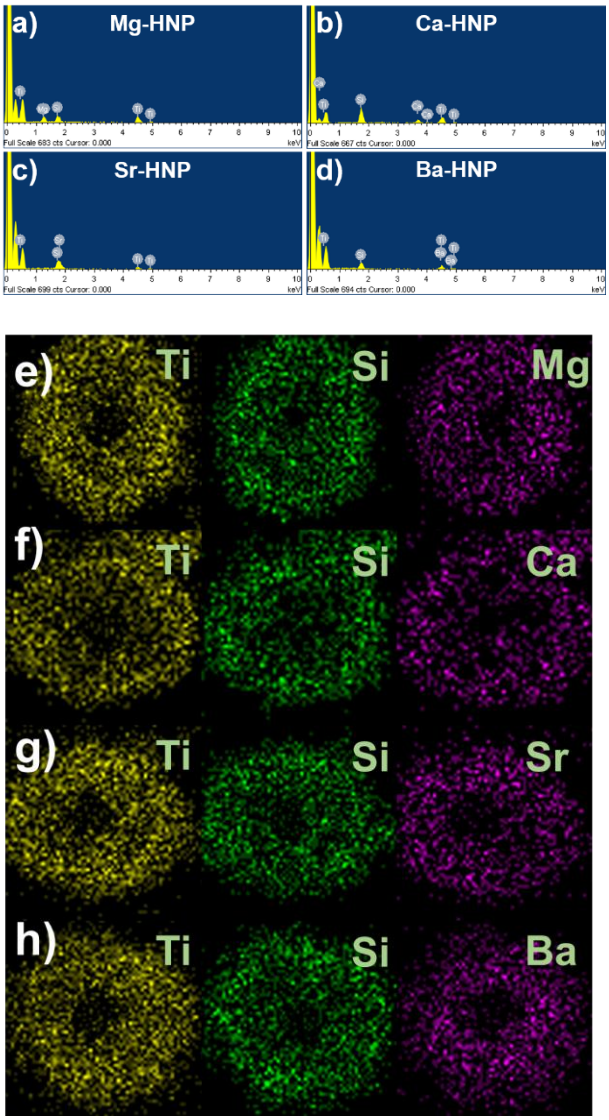

Figure 34. EDS spectra of a) Mg-HNP, b) Ca-HNP, c) Sr-HNP, and d) Ba-HNP. EDS mapping of e) Mg-HNP, f) Ca-HNP, g) Sr-HNP, and h) Ba-HNP

Table 2. Variation of atomic % of Si, Ti, and divalent metal ion of Mg-HNP, Ca-HNP, Sr-HNP, and Ba-HNP.

Sample	**Atomic ratio (%)**		
	Si	Ti	Metal ion
Mg-HNP	33.52	46.25	20.23
Ca-HNP	35.18	44.85	19.97
Sr-HNP	34.90	45.04	20.06
Ba-HNP	35.61	43.58	20.81

Formation of the HNPs were performed by X-ray photoelectron spectroscopy (**Figure 35**). The AEM doped HNP deconvoluted as silica and silicate peaks at 103.1eV (green) and 101.7 eV (blue), respectively [69, 70]. Furthermore, Ti 2p signals were displayed titania (458.9 eV and 465.2 eV; green) and titanate (458.3 eV and 463.8 eV; red) [71-75]. Also, the deconvoluted silicate and titanate signals were observed. Consequently, it could be conclude that silica, silicate, titania, titanate constituted the HNPs (HNP: SiO_2 and TiO_2, Mg-HNP: SiO_2, TiO_2, $MgSiO_3$, and $MgTiO_3$; Ca-HNP: SiO_2, TiO_2, $CaSiO_3$, and $CaTiO_3$; Sr-HNP: SiO_2, TiO_2, $SrSiO_3$, and $SrTiO_3$; Ba-HNP: SiO_2, TiO_2, $BaSiO_3$, and $BaTiO_3$) [76, 77]. By using metal hydroxide, the Mg-HNP, Ca-HNP, Sr-HNP, and Ba-HNP were successfully fabricated.

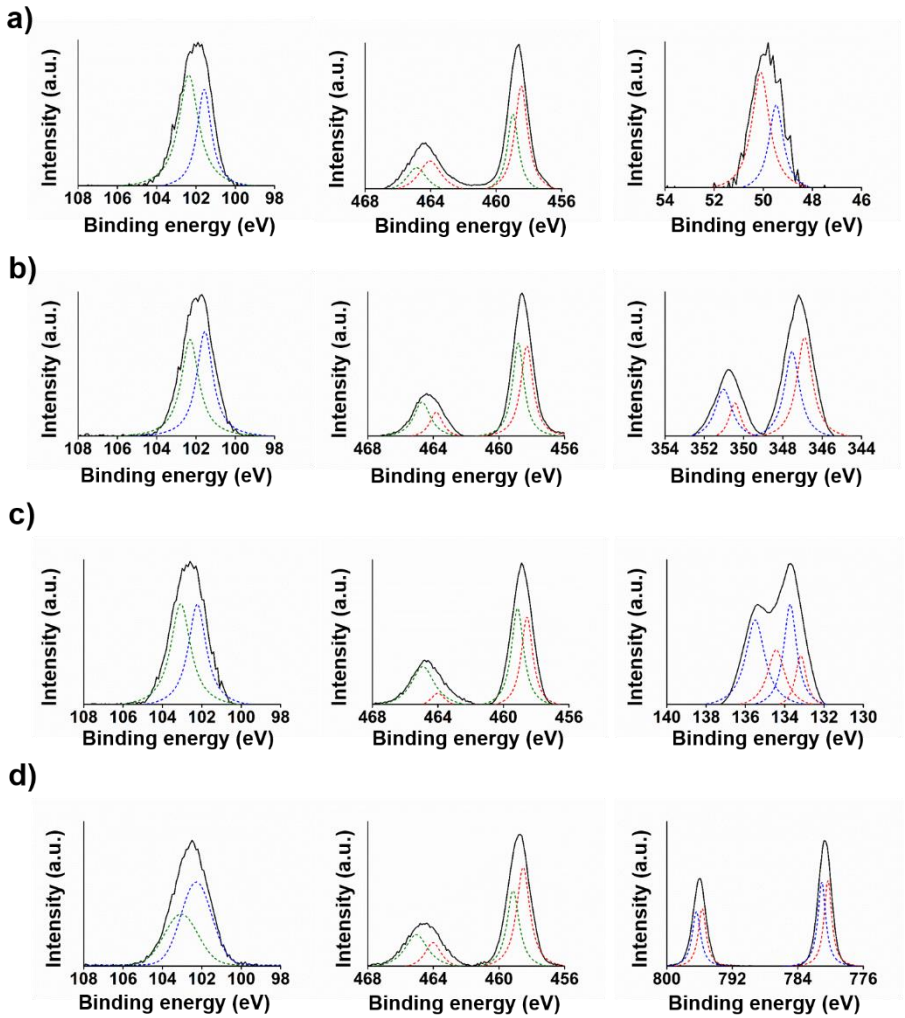

Figure 35. XPS spectra of a) Mg-HNP, b) Ca-HNP, c) Sr-HNP, and d) Ba-HNP. (from left to right: Si 2p, Ti 2p, metal ion 3d spectra (Mg, Ca, Sr, and Ba); deconvoluted components-green: SiO_2 or TiO_2; blue: $MgSiO_3$, $CaSiO_3$, $SrSiO_3$, and $BaSiO_3$; red: $MgTiO_3$, $CaTiO_3$, $SrTiO_3$, and $BaSiO_3$).

In this thesis, PC-12 cells were used for demonstrate the neuronal differentiation effect of the HNPs, because PC-12 cells were generally used in neuronal development research [78, 79].

Prior to investigate the neuronal development effect, the cytotoxicity of the HNPs toward PC-12 cells were evaluated. By ATP luminescent assay, the intercellular ATP content was measured by comparing the intensity changes at 560 nm and the ATP related cell viability was calculated and presented in **Figure 36a**. Many systems used this method for measuring cell viability. The cell viability of the PC-12 cells exhibited as 90 %, 97 %, 86 %, 84 %, and 81 % when treated with only NGF, Mg-HNP, Ca-HNP, Sr-HNP, and Ba-HNP, respectively. When incubated for 3 days, the cell toxicity showed less than 20 %, which means HNPs had low toxicity toward PC-12 cells [80, 81].

The intercellular reactive oxygen species (ROS) was detected by H_2DCFDA dye [82, 83]. In this manuscript, PDT induced total cell damage (including mitochondrial damage) was investigated by H_2DCFDA [84-86]. The H_2DCFDA was oxidized by intercellular ROS and emitted green fluorescence [87]. In general, H_2DCFDA was used for determining intercellular ROS generation. The HNPs induced cell

damage could be quantified by this generated H_2DCFDA. In **Figure 36b**, the ROS generation was increased proportionally with incubation time. There was insignificant H_2DCFDA fluorescence change in PC-12 cells. HNP treated cells showed low cell damage levels indicating that HNPs are adequate for neuronal development system even with 3 days of particle incubation.

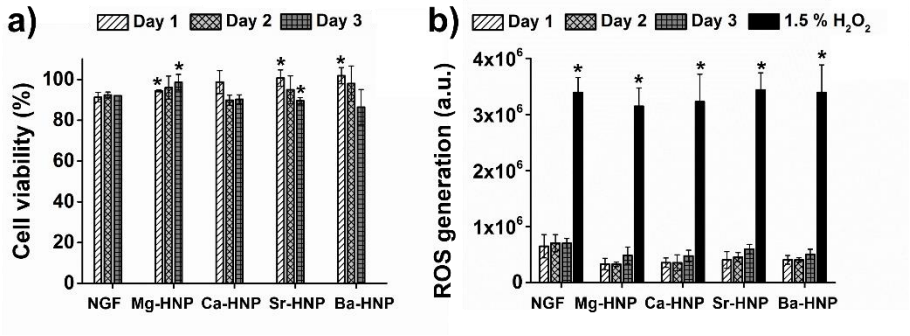

Figure 36. a) Cell viability and b) ROS generation of the PC-12 cells treated with HNPs. The experiments were conducted with time dependence. Cells were irradiated after 24 h incubation of nanoparticles. Values exhibit mean ± SD and each experiment was performed in triplicate. *Statistically significant difference from negative control.

3.2.2 Application for neuron development promoter

To investigate the effect of Mg-HNP, Ca-HNP, Sr-HNP, and Ba-HNPs cooperated with nerve growth factor on mammalian neuron differentiation, PC-12 cells were used as a model cell line [88]. These cells were differentiate like sympathetic neuron cells in response to neurotropic molecuels, such as NGF and EGF [89, 90]. Recently, inorganic nanoparticles had gained many attention as a these neurotropic molecule delivery agent [91]. However, little is known about the neuronal development effect induced by the alkaline earth metal ion doped HNPs. To the best of out knowledge, this is the first investigation of the facilitation of the neurite outgrowth by HNPs. The PC-12 cells were treated with antibody against β-tubulin (class Ⅲ; anti-β-tubulin (Ⅲ)). The anti-β-tubulin was generally used for observing neuronal filament [92, 93]. **Figure 37** shows immune fluorescent images of PC-12 cells treated with HNPs-NGF. Morphological changes in the cells were enchanced by increasing particle treatment time. The neurite development efficiency was maximized neurite development under Sr-HNP condition at 3 days of treatment time. The alkaline earth metal ion

doped-HNPs facilitated the development of PC-12 cells in coorporation with NGF.

Statistical results were obtained from immufluorescent images to investigate the percentage of differentiated cells and average neurite length (**Figure 38**). The neurite length and differentiation efficiency was demonstrated as it is dependent to the HNPs type. The average of neurite length was increasing in this order: Sr-HNP > Ba-HNP > Ca-HNP > Mg-HNP. Furthermore, Sr-HNP treated PC-12 cells exhibited 2.39 times of higher neuron elongation efficiency compared to only NGF treated cells. Whereas, in terms of the percentage of differentiation, the consequence was slightly different from the average neurite length result. The differentiation efficiency was highest in the order of Sr-HNP > Mg-HNP > Ca-HNP > Ba-HNP. In Sr-HNP treated cells, the differentiation efficacy was 2.27 times higher than only NGF treated cells.

Consequently, the neuronal development efficiency (the average neurite length and the percentage of differentiated cells) was enhanced by using metal ion doped HNPs [94, 95]. Sr-HNP showed high neuronal development effect in both neurite length and development percentage. While, Ba-HNP exhibited high neurite length elongation efficacy, it had lowest differentiation efficiency. Mg-HNP involved least in neurite

elongation process, but showed high effect in differentiation efficiency. In comparison with other metal ion doped HNPs, Ca-HNP treated cells revealed low neuronal development effect for both neurite length and differentiation percentage. Judging from this data, Mg, Ca, Sr, and Ba plays different roles in facilitating neuronal differentiation [96, 97].

To compare stimulating ability for neurite outgrowth, control experiment was conducted in NGF negative condition. In **Figure 39**, the result was exhibited as neither neuritis nor morphological changes in only HNPs treated PC-12 cells. Therefore, it could be concluded that the HNPs directly promote neurite outgrowth, but it could effect on neurite development in cooperation with NGF.

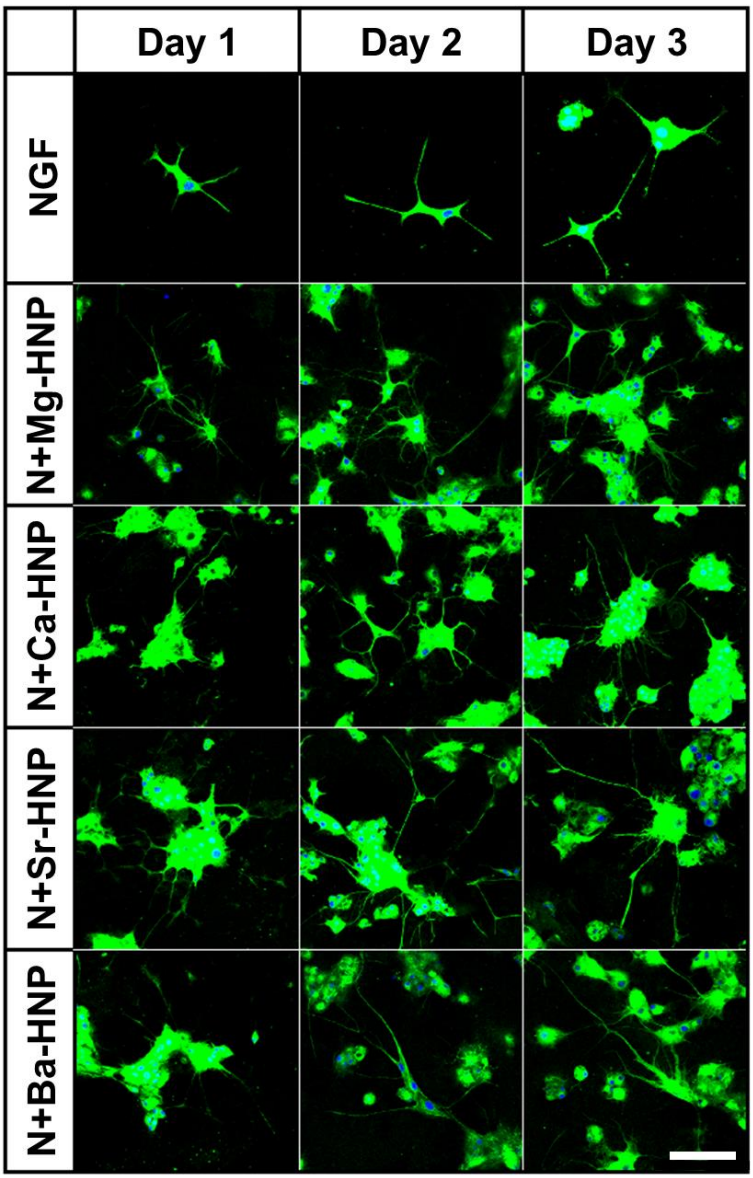

Figure 37. Livecell images of only NGF, Mg-HNPs, Ca-HNP, Sr-HNP, and Ba-HNP (green: beta-tubuline FITC fluoresence, blue: cell nucleus).

PC-12 cells were treated with nanoparticles and nerve growth factor (NGF) for 1day, 2 day, and 3day (Scale bar: 100 μm).

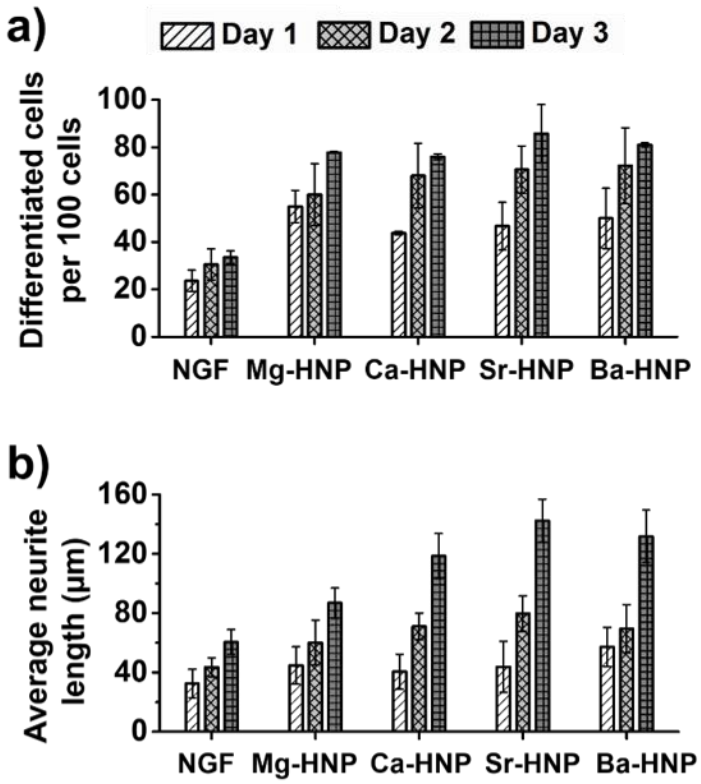

Figure 38. Average cell length of PC-12 cells in a condition of NGF and different types of nanoparticle. Values exhibit mean ± SD and each experiment was performed in triplicate.

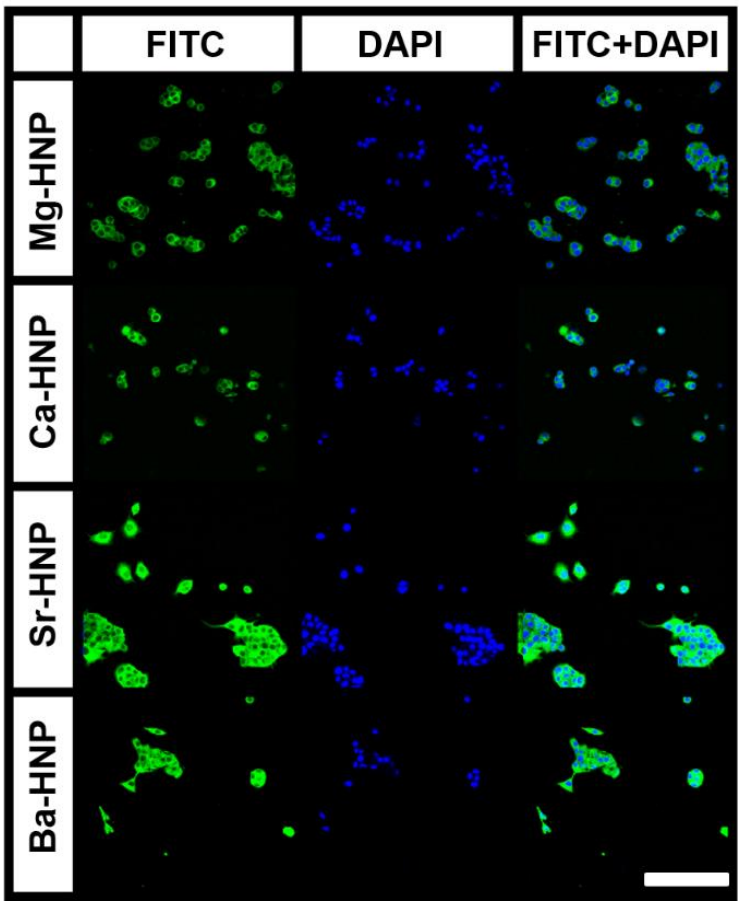

Figure 39. Livecell images of Mg-HNPs, Ca-HNP, Sr-HNP, and Ba-HNP (green: beta-tubuline FITC fluoresence, blue: cell nucleus). PC-12 cells were treated with nanoparticles for 3day without nerve growth factor (NGF) (Scale bar: 100 μm).

It is hypothesized that the localization of the intercellular HNPs is the key factor that differentiates PC-12 cells. TEM images of the intracellular HNPs in PC-12 showed that HNP nanoparticles were internalized into the cells (**Figure 40**). The intracellular particles maintained their original shape, and most of the particles were located inside the endosome or secretary granule. Internalization of the particles into the cells did not induce serious cell damage and cell toxicity. Furthermore, the pH level of the endosome and secretary granule is pH 5.5, which weak acid condition would lead partial ionization of HNPs and release metal ions into the cytosol [98, 99]. The pH related metal ion release was observed by inductively coupled plasma mass spectrometry (ICP-MS). In a condition of pH 5.5, about 32 % of the metal ion was released out from HNPs after 24 h. At pH 7 phosphate buffer saline solution, the metal ion was released very few. By this result, it could be concluded that the dissolved metal ion would effectively delivered to the inner cell and activate the neuronal development.

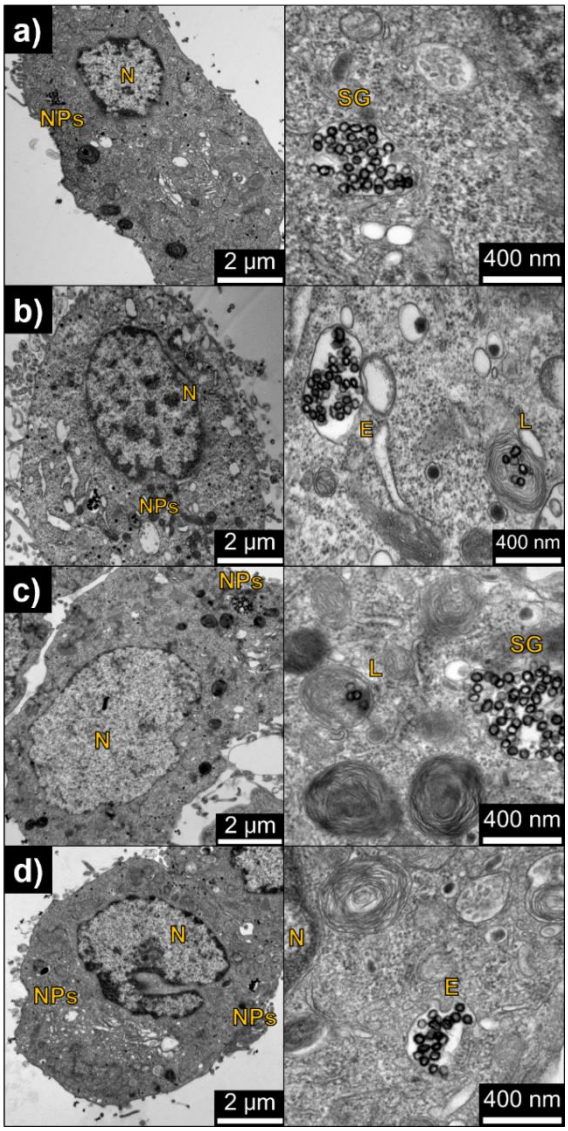

Figure 40. Microtoming images of PC-12 cells with a) HNP, b) Mg-HNP, c) Ca-HNP, d) Sr-HNP, and e) Ba-HNPs of 25 µg mL^{-1}. (Abbreviation: N: nucleus; SG: secretary granule; E: endosome; NP:nanoparticle)

As a response to the leached metal ion, PC-12 inner cell triggered mitogen activated protein kinease (MAPK) [100-103]. A mitogen is a chemical substance that encourages a cell to commence cell division, triggering mitosis [104]. A mitogen is usually some form of a protein. Mitogenesis is the induction (triggering) of mitosis, typically via a mitogen. Mitogens trigger signal transduction pathways in which mitogen-activated protein kinase (MAPK) is involved, leading to mitosis. The signal transduction pathway is the transmission of a molecular signal in the form of a chemical modification by recruitment of protein complexes along a pathway that ultimately triggers a biochemical event in the cell. Signal transduction occurs when an extracellular signaling molecule activates a specific receptor located on the cell surface or inside the cell. In turn, this receptor triggers a biochemical chain of events inside the cell, which known as a signaling cascade that elicits a response. The expression of MAPK signaling cascades including c-jun N-terminal kinases (JNK), extracellular signal regulated kinases (ERK 1/2), protein kinase 38 (p38) were analyzed in **Figure 41**. Furthermore, it could be conducted an experiment for expression of tropomyosin receptor kinase A (TrkA), which was specific NGF binding receptor. As mentioned

above, the released metal ion activate JNK, p38, and ERK1/2 by phosphorylation; pJNK, pp38, pERK. The phosphorylated proteins would develop cell neuronal differentiation. The expression of pp38, pJNK, pERK, TrkA expression level was observed by flow cytometry. The TrkA was expressed in all NGF treated cells. In Mg-HNPs incubated cells, the pJNK level was higher than Ca-HNP, Sr-HNP, and Ba-HNP incubated cells. The pJNK level was related to the cell survival in neuronal differentiation system. The result was observed in ATP assay and confocal images of β-tubulin(Ⅲ). For Ca-HNP, Sr-HNP, and Ba-HNP treated cells, the pp38 and pERK level was higher than only NGF and Mg-HNP treated cells. The pp38 was related to the cell death and the pp38 level elevated as increment of HNP treatment time. The same tendency was exhibited in pERK leve. The pERK was a key protein in neuronal development and differentiation. Upon neuronal development, the cell adhesion was weaken as neurite length increases. In this reason, the pp38 level was consistent with the pERK level. Collectively, this finding revealed that enhanced neuronal differentiation by HNPs was originated form MAPK signaling cascades (**Figure 42**).

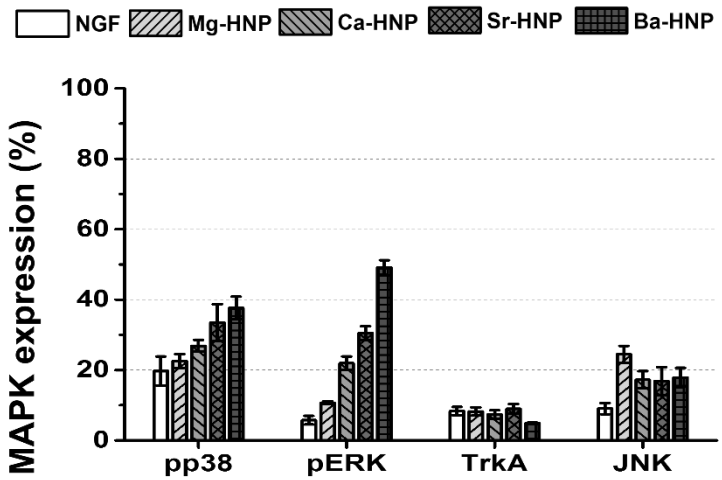

Figure 41. Effect of Mg-HNP, Ca-HNP, Sr-HNP, and Ba-HNPs for PC-12 cells.

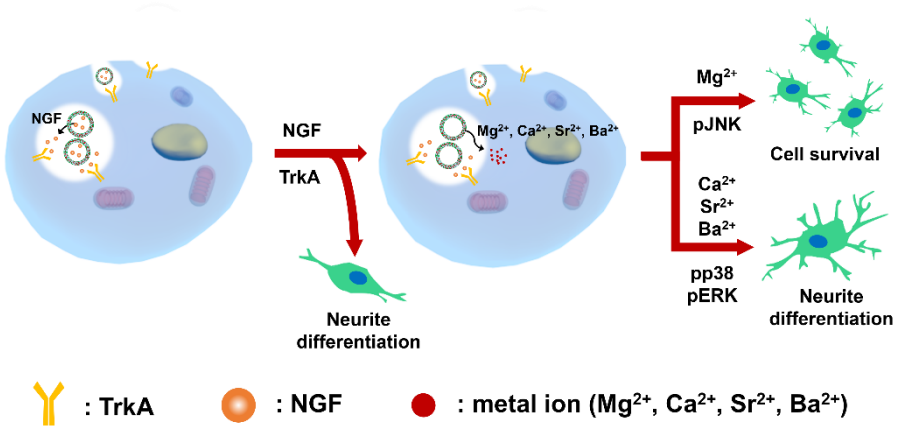

Figure 42. Proposed mechanism of promoting effects of HNPs on the neuronal differentiation.

3.3. GQD/PPy coated hollow nanoparticles for bioimaging and drug delivery

3.3.1 Fabrication of GQD/PPy coated hollow nanoparticles

Figure 43 is a schematic diagram for fabrication of the graphene quantumdot (GQD) decorated hollownanoparticles coated with polypyrrole (GQD/PPy-HNP). SiO_2 HNPs, fabricated by stöber method, were covered with TiO_2 shell to prepare SiO_2/TiO_2 core/shell nanoparticle (CSNP). Then, the CSNP solution was mixed with ammonium hydroxide solution. By this process, the CSNP turned into hollow nanoparticles (HNPs), associated with sonication mediated etching redeposition (SMER) method (**Figure 44**) [105]. Following method allowed for uniform control of hollownanoparticle size and distribution. The synthesized HNPs were used as a drug carrier for dexamethasone (DEX). The HNP solution was mixed with 0.1M of DEX solution and stirred for 24 h to loading DEX into HNP. After fabricating HNPs, 0.1M of ferric chloride ($FeCl_3$) solution were added for introducing initiator to the HNPs' surface. After introducing the initiator to the HNPs, pyrrole monomer was dropped to polymerize polypyrrole

(PPy-HNP) (**Figure 44c**). Furthermore, the ferric chloride introduced HNPs were mixed with pyrrole monomer and 10 ng of GQD to fabricate GQD/PPy-HNP. By adding GQD to the PPy polymerization process, the GQD embedded PPy shell has been successfully fabricated (**Figure 44d**) [106, 107].

Transmission electron microscopy (TEM) images and electrophoretic light scattering (ELS) data confirmed that the GQD had an average diameter of *ca.* 5.7 nm (**Figure 44a**). The diameter of HNP was 50 nm with uniform size and narrow size distribution. After PPy coating, the diameter of the HNPs increased by 10 nm. Furthermore, GQD/PPy coated HNPs exhibited *ca.* 70 nm of diameter, which was 20 nm increased shell thickness in comparison with 50 nm HNPs diameter. The increased shell thickness of GQD/PPy-HNP was caused by GQD enhanced PPy polymerization [108].

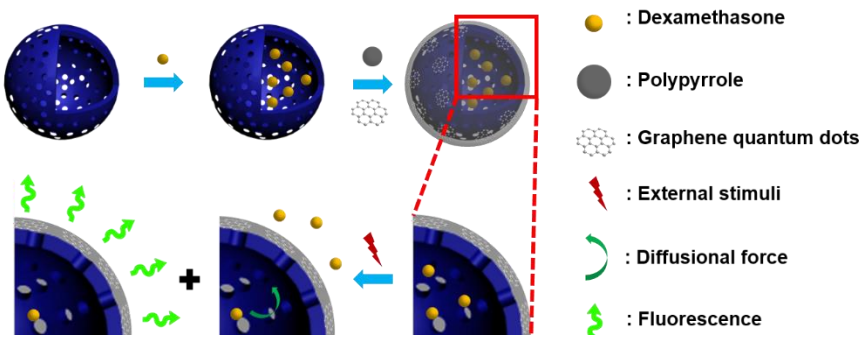

Figure 43. Schematic illustration of stimuli responsive drug release and bio imaging available GQD/PPy-HNP.

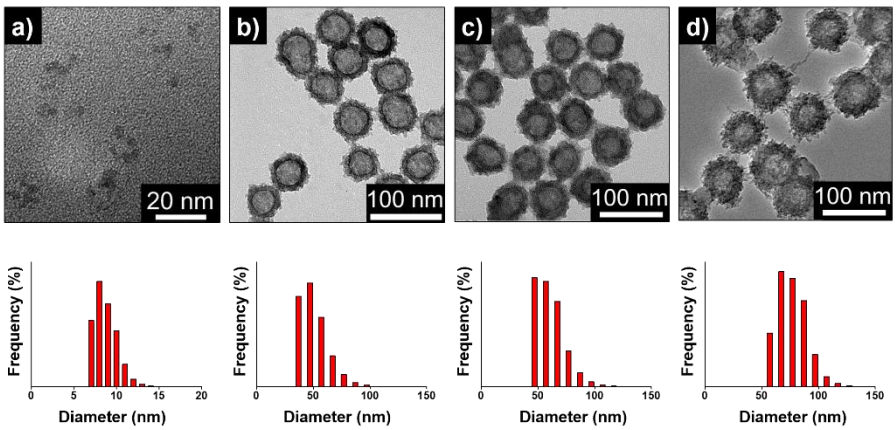

Figure 44. TEM images and size distribution histograms of a) GQD, b) HNP, c) PPy-HNP, and d) GQD/PPy-HNP.

The chemical composition of the hybrid materials was confirmed by XPS. **Figure 45a** shows the complete spectra over the range of 0 to 1000 eV. Theses spectra demonstrated that Si, Ti, C, N, O atoms were present in PPy-HNP and GQD/PPy-HNP, whereas Si, Ti, O were present in the HNPs. **Figure 45b** exhibits the C 1s band of PPy-HNP and GQD/PPy-HNP, deconvoluted into several components. The peaks at 288.9, 286.6, 285.9, and 284.2 eV were corresponding with C=O, C-OH, C-N, and C-C components in the polypyrrle structure. For GQD/PPy-HNP nanoparticles, the C-OH components were increased as a result of GQD additives. The N 1s peaks for two PPy types were shown in **Figure 45c**. For PPy-HNP, three deconvoluted peaks were attributed to the N component in the pyrrole structure: 400.7 eV for 399.6 eV for -N-, and 398.2 eV for neutral -N= [109, 110]. In **Figure 45c**, four deconvoluted peaks were demonstrated for the N component in GQD/PPy-HNP nanoparticles: 402.1 eV for –N=+, 400.7 eV for -N-+, 399.6 eV for -N-, and 398.2 eV for neutral -N= [111-113]. As a result, it could be concluded that by adding GQD to the PPy synthesis process, a new structure component of PPy had been formed.

Fourier transform infrared spectroscopy (FT-IR) confirmed the synthesis

(**Figure 46a**). The spectrum of the HNPs had characteristic peaks at 952, 1075, and 1402 cm^{-1} corresponding to Si–O–Ti vibrations, Si–O stretching, and Si–O stretching overtone vibrations, respectively [114, 115]. HNP–PPy had a characteristic pyrrole paeks at 1030 cm^{-1}, 1148 cm^{-1} 1580 cm^{-1}, 3483 cm^{-1}, corresponding to N-H and C-H deformation vibrations, C=N in plane vibration, and N-H stretching [116, 117]. The characteristic peaks of GQD/PPy-HNP was exhibited at 1050 cm^{-1} (C-O stretching vibrations in epoxide), 1218 cm^{-1} (C-OH stretching vibration), 1395 cm^{-1} (O-H deformations in the C-OH groups), 1536 cm^{-1} (asymmetric CO^2 stretching). The increased intentiities of the C=C stretching band of the C=C-N at 1621 cm^{-1}, which result demonstrated the successful GQD embedded PPy surface coating for the HNP [118-120]. The peak assignments were summarized in **Table 3**. On the basis of these data, PPy and GQD successfully modified the surface of the HNP.

Figure 46b displays representative absorbance spectra of GQD. UV-visible spectra showed an absorbance peak at 360 nm. The fluorescence spectra showed optimized excitation an emission wavelength at 360 nm and 520 nm.

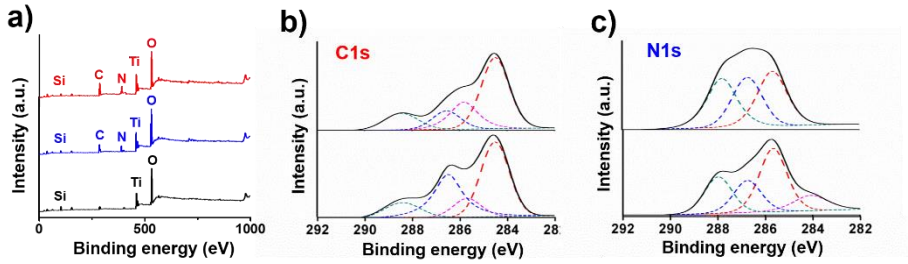

Figure 45. a) XPS spectra of HNP (black), PPy-HNP (blue), and GQD/PPy-HNPs (red). b) Enlarged C 1s and N 1s spectrum of HNPs (up: PPy-HNP and bottom: GQD/PPy-HNP).

Table 3. Peak assignment of HNP, PPy-HNP, and GQD/PPy-HNP.

Materials	Wavenumber (cm^{-1})	Assignments
HNP	1402	Si-O overtone
	1075	Si-O stretching
	952	Si-O-Ti
PPy-HNP	3483	N-H stretching
	1580	C=N in plane vibration
	1148	C-H deformation vibration
	1030	N-H deformation vibration
GQD/PPy-HNP	1621	C=C stretching band
	1536	asymmetric CO_2 stretching
	1395	O-H deformations
	1218	C-OH stretching vibration
	1050	C-O stretching vibration

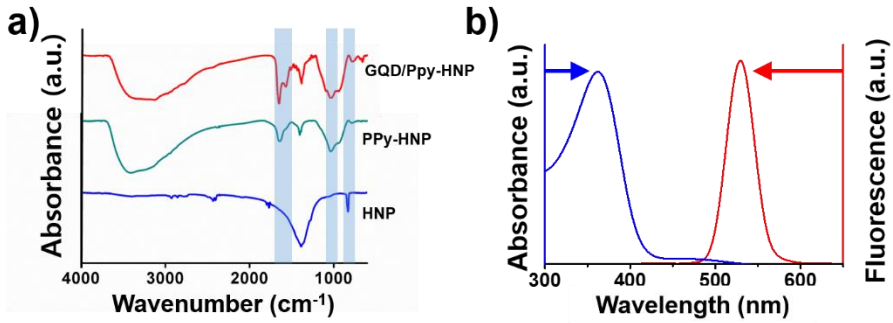

Figure 46. a) FT-IR spectra of HNP, PPy-HNP, and GQD/PPy-HNP. b) UV-vis absorprion spectra and fluorescence emission spectra of GQDs.

3.3.2 Application for bioimaging system

On the basis of the UV and PL data, the bioimaging ability of the GQD/PPy-HNP was systematically investiaged in MCF-7 cells. The fluorescence image of GQD/PPy-HNP treated cells and their DIC, fluorescence images were shown in **Figure 47**. When MCF-7 cells were treated with the PPy-HNP (without GQD), the PPy-HNP showed no fluorescence in MCF-7 cells. While, the GQD and GQD/PPy-HNP was successfully internalized into the cells and exhibited uniform and high green fluorescence, indicating the GQDs still had high fluorescence after incorporated with PPy [121-123]. Furthermore, according to the fluorescence images, PPy-HNP, GQD, and GQD/PPy-HNP showed insignificant change in cell shape and induced any damage to the cell.

A flow cytometry analysis was performed to quantify the intracellular GQD (**Figure 48**) [124]. When the cells were treated with 100 μg mL^{-1} of GQD/PPy-HNP, the fluorescence of the GQD/PPy-HNP (fluorescence mean intensity: 6.04) exhibited as similar to that of the pristine GQD (fluorescence mean intensity: 6.76). Consequently, the 200 μg mL^{-1} of GQD/PPy-HNP incubated cells showed slightly higher fluorescence intensity in comparison to the pristine GQD (fluorescence mean intensity:

7.62). Furthermore, as GQD/PPy-HNP concentration increased from 100 μg mL^{-1} to 500 μg mL^{-1}, the median value also increased from 6.04 to 11.68. These results indicated that GQD/PPy-HNPs were successfully internalized in MCF-7 cells and demonstrated potentiate as a bio imaging agent [125, 126].

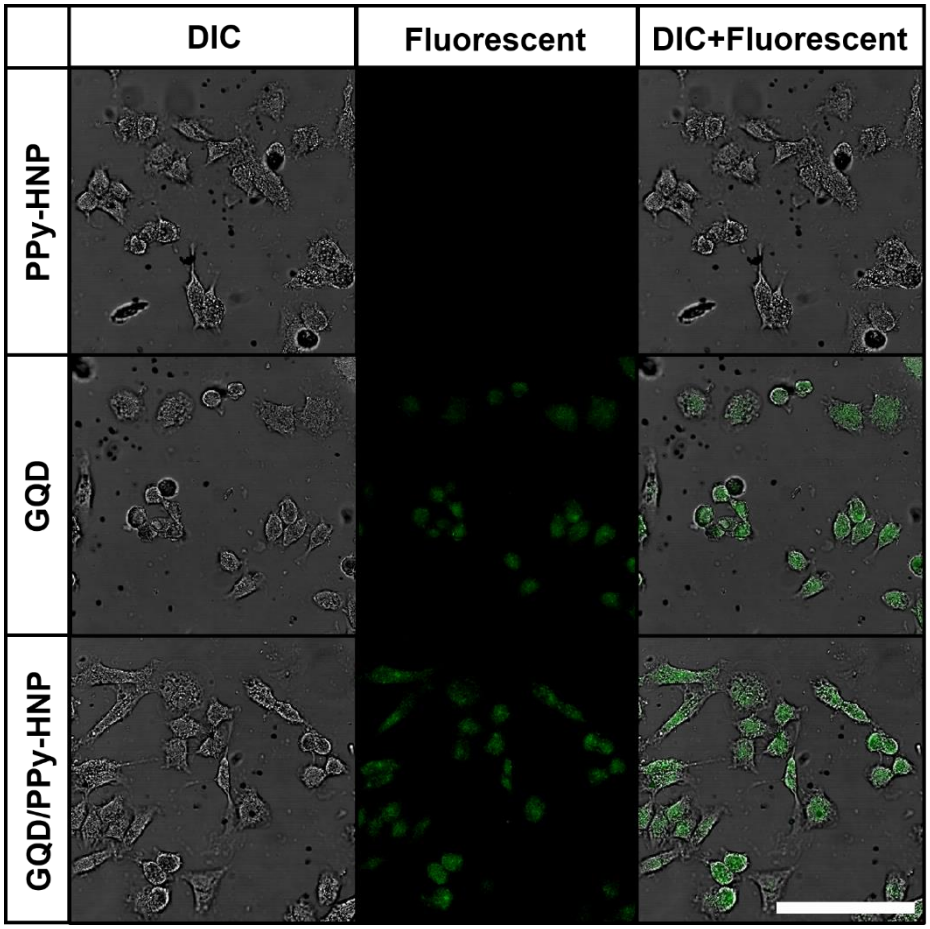

Figure 47. Fluorescence images of MCF-7 cells treated with PPy-HNP, GQD, and GQD/PPy-HNP (0.05 mM). From left to right: DIC images, fluorescent images, and DIC and fluorescent merged images of MCF-7 cells treated with 50 ng mL^{-1} of GQD and 50 μg mL^{-1} of PPy-GQD and GQD/PPy-HNP. (Scale bar: 100 μm)

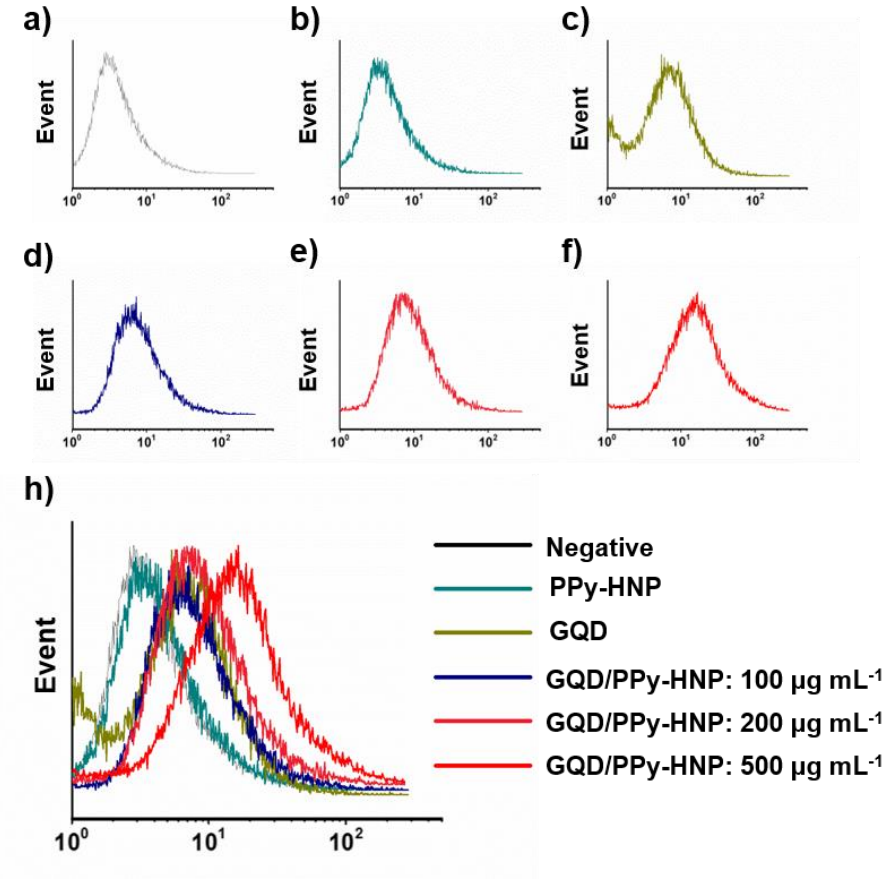

Figure 48. Flow cytometric analyses of MCF-7 cells with incubation of a) Negative, b) PPy-HNP, c) GQD, d) 100 µg mL^{-1} of GQD/PPy-HNP, e) 200 µg mL^{-1} of GQD/PPy-HNP, f) 500 µg mL^{-1} of GQD/PPy-HNP incubated for 24 h.

3.3.3 Application for stimuli-responsive drug release

Cyclic voltammetry (CV) was used to investigate the charge-transfer capacity through the electrodes after surface modification with PPy and GQD/PPy shell [127, 128]. The schematic mechanism of the electrical stimuli responsive DEX release was presented in **Figure 49a**. The microelectrode was swept through as potential of -0.9 V to 0.5 V at a scan rate of 100 mV s^{-1} [129, 130]. During CV, the coating underwent reduction and oxidation due to movement of counterions in and out of the PPy coating. In **Figure 49b**, the oxidization and reduction reactions involved current flow through PPy that appeared as peaks on the CV graph. Furthermore, when the PPy shell was incorporated with the GQD, the GQD/PPy-HNP showed insignificant changes in CV curve. By this result, it could be concluded that after incorporating GQDs in PPy shell, the characteristic electrical property of PPy was still unchanged and maintained as well.

After investigate the CV graph of the PPy-HNP and GQD/PPy-HNP, the drug loading and drug release property of the nanoparticles had been confirmed [131-133]. Electrically controlled release of DEX molecules could be achived by utilizing the unique redox properties of the DEX

loading GQD/PPy-HNP nanocomposite [133-135]. To evaluate the drug releasing performance of the GQD/PPy-HNP, voltage pulses were applied through the HNPs immersed in 0.1 M PBS, and release solution was analyzed by UV-visible absorbance spectroscopy to quantify the amount of DEX from the GQD/PPy-HNP [130, 136]. The maximum loading capacity of HNPs was investiaged by observe the released DEX upon the aggressive stimulation. The loading capacity of the HNP, PPy-HNP, and GQD/PPy-HNP were demonstrated as 25.5 μM, 15.3 μM, and 20.4 μM, respectively. The high loading capacity revealed thet great advantages of HNPs as a dexamethasone loading carrier and suitability for delivery agents. To further analyze the stimulus responsive drug release property, the amount of the released DEX was measured by UV-Vis spectroscopy. **Figure 49c** shows the percentage of the released DEX from the HNPs after applying 10000 cycle of electrical stimulus (-2 V for 5 s, followed by 0V for 5 s) [137]. After 3000 stimulation cycle, the drug release profile reached a plateau, suggesting that no more drug could be released from the GQD/PPy-HNP. Small quantities of DEX released from the PPy-HNP and GQD/PPy-HNP after sufficient stimulation. While, no observable amount of DEX was diffused from the HNPs in the absence of stimulation. By comparing the DEX release study,

it had been demonstrated that the released dose of the drug could be controlled by electrical stimulus not diffusion. The mechanism of DEX release from PPy shell upon electrical stimulus has been demonstrated in **Figure 50**.

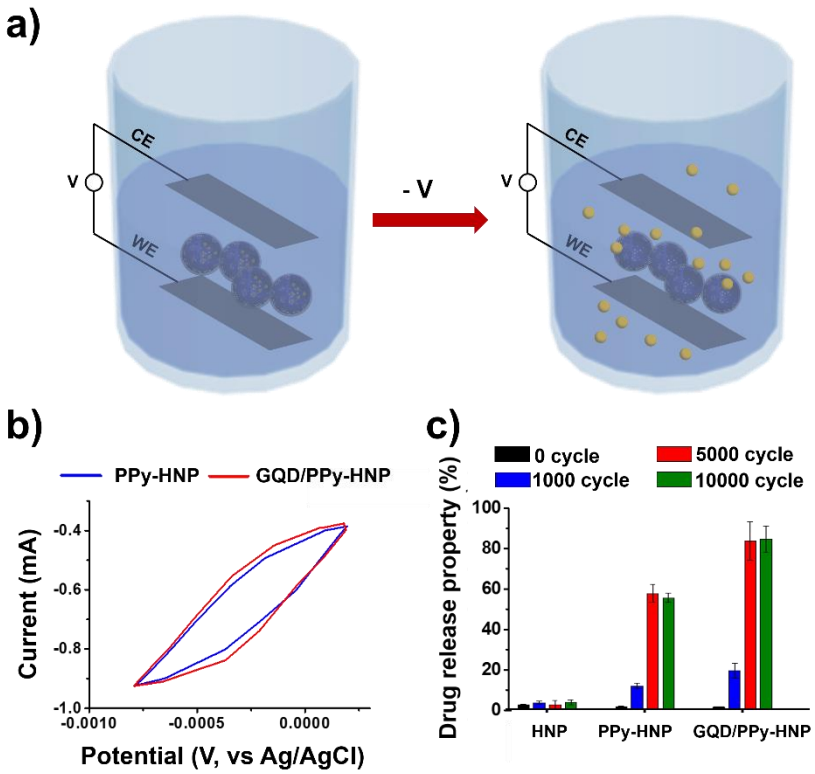

Figure 49. a) Schematic illustration of the controlled release of dexamethasone from PPy-HNP in a neutral electrical condition. b) CV of PPy-HNP and GQD/PPy-HNP. c) Cumulative DEX release from HNP, PPy-HNP, and GQD/PPy-HNP after 0 cycle, 1000 cycle, 5000 cycle, and 10000 cycle. Values exhibit mean ± SD and each experiment was performed in triplicate.

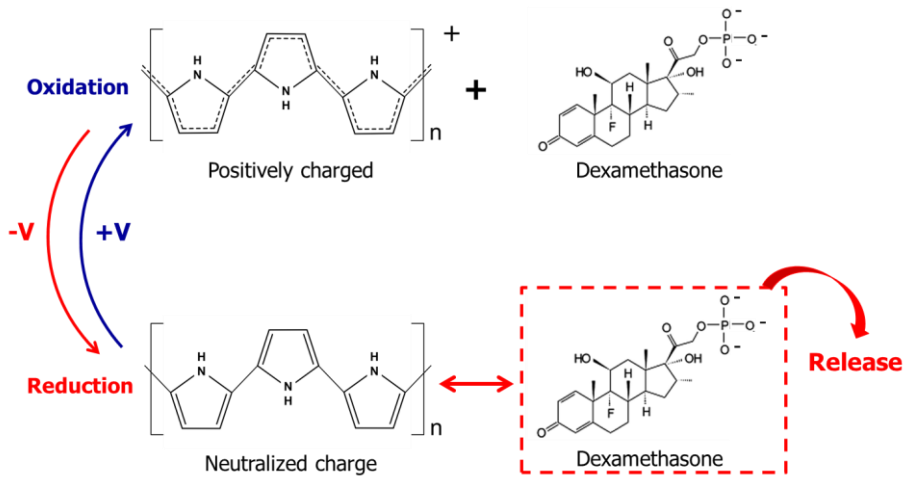

Figure 50. Mechanism of electrical stimulus responsive DEX release from PPy.

The bio activity of the released drug was assessed by addition of solutions containing DEX released from GQD/PPy-HNP to cluture medium of MCF-7 cell and evaluation of the extent of cell damage [138-140]. MCF-7 cultures were exposed to the release solution. The drug release solutions were obatained using the aggressive stimulation paradigm (-0.5 V for 5 s, 0 V for 5 s, 1000 cycles). In **Figure 51**, the cell damage of the DEX solution treated MCF-7 cells were observed. **Figure 51** shows fluorescent images of cells treated with the DEX solution in which the cells stained with PI. Unstained cells defined viable cells, and red fluorescent labels were classified as necrotic cell damage. In GQD/PPy-HNP treated samples, the red fluorescent cells were increased as proportion to the stimulation cycle increment (DEX solution concentration increment). In addition, the DEX solution released from PPy-HNP treated MCF-7 cells exhibited some extent of cell damage. While, no noticeable cell damage was observed for HNP released DEX contained solution treated sample. These result demonstrated that the DEX solution released from GQD/PPy-HNP could induce intercellular damage [136, 141-143].

After investiage the fluorescent images, the cell damage was observed

by adenosine triphosphate (ATP) and reactive oxygen species (ROS) assay. By ATP luminescent assay, the intercellular ATP content was measured by comparing the intensity changes at 560 nm and the ATP related cell viability was calculated and presented in **Figure 52a**. There was no fluorescence disturbance for DEX (emission: 600 nm- 700 nm with ATP luminescent dye). Many cytotoxicity test used this method for measuring cell viability. The ATP based cell viability showed similar result when compared with the fluorescent images. Therefore, it could be concluded that ATP assay tested cell viability were trustworthy and reliable cell viability test. These ATP assay result indicated an effective MCF-7 cell damage inducing ability of DEX solution released from PPy-HNP and GQD/PPy-HNP after 1000 cycle of stimulation.

The intercellular reactive oxygen species (ROS) was detected by H_2DCFDA dye. In this thesis, DEX induced total cell damage was investigated by H_2DCFDA. The H_2DCFDA was oxidized by intercellular ROS and emitted green fluorescence. In general, H_2DCFDA was used for determining intercellular ROS generation. The DEX induced cell damage could be quantified by this generated H_2DCFDA. In **Figure 52b**, the ROS generation was increased proportionally with stimulation cycle in PPy-HNP and GQD/PPy-HNP. There was

insignificant H_2DCFDA fluorescence change in the DEX solution released from HNP treated cells. In this respect, without surface coating of HNP with PPy and GQD/PPy, there was ineffective in DEX release for damaging MCF-7 cells even under electrical stimulation. From these results, it could be concluded that GQD/PPy-HNP had selectively act on stimulus responsive for electrical field and effectively destruct MCF-7 cell.

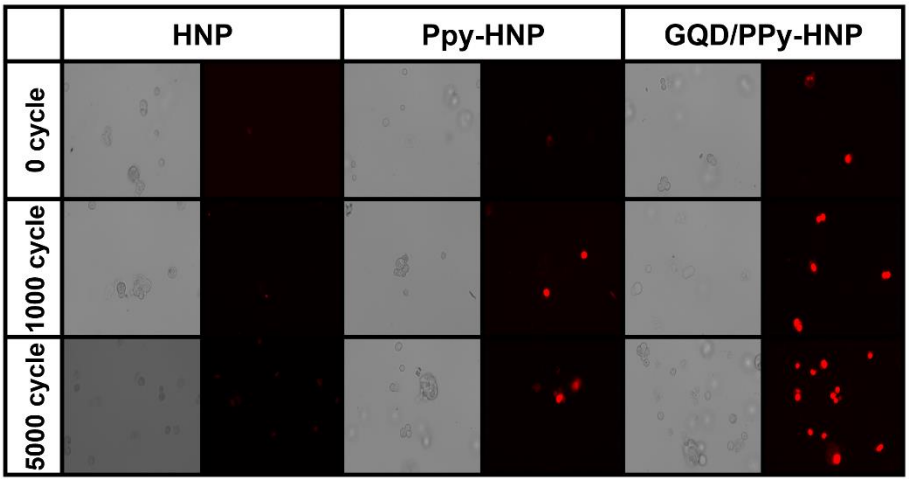

Figure 51. Livecell differential interference contrast (DIC) and fluorescence images of DEX solution released from HNP, PPy-HNP,and GQD/PPy-HNP treated MCF-7 cell. From up to the bottom, the cycle time is 0, 1000, and 5000 μg mL^{-1}. Cells were stained with propidium iodide (PI) for visualing necrosis of cells. DIC images were taken at the same time, corresponding to the fluorescence images (scale bar: 100 μm).

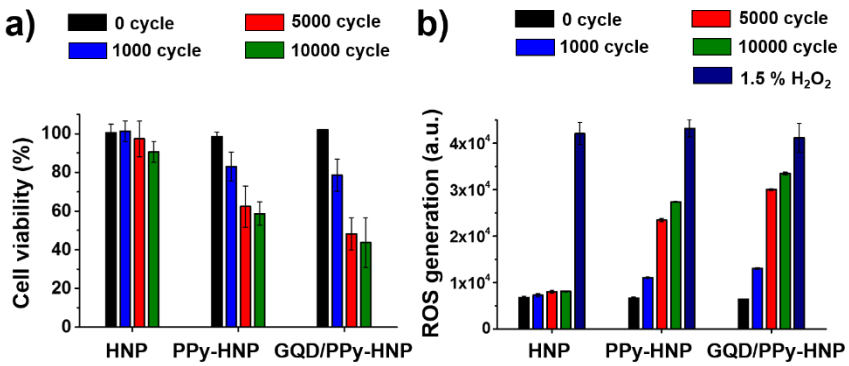

Figure 52. a) Cell viability and b) ROS generation of the MCF-7 cells treated with DEX solution released from HNP, PPy-HNP, and GQD/PPy-HNP. The experiments were conducted with cycle time. Cells were stimulated after 24 h incubation of nanoparticles. Values exhibit mean ± SD and each experiment was performed in triplicate.

4. Conclusion

The subtopic is concluded in the view point of each subtopic as follows:

1. Monodisperse 50 nm HNPs in diameter, were used as a nanocarrier to load photosensitizer PpIX for PDT, and the surface was further functionalized with GO for PTT and efficient drug release. The NIR laser was exploited for activating GO to generate heat and further leading to release PpIX into the cells. The visible light was used as a PDT light source instead of a conventional laser to minimize photodamage to normal cells. Under the same experimental conditions, both NIR laser and visible light irradiated cell viability decreased to dramatically compared with for only visible light or NIR irradiated cells. Therefore, the combined GO–HNP–PpIX/NIR laser/visible light system offers a new direction for synergistic effect PTT and PDT.

2. Alkaline earth metal ion-doped hollow nanoparticles were fabricated using sol-gel and sonication mediated etching and redeposition (SMER) method and alkaline earth metal hydroxide solution treatment to

fabricate neuronal development in coorperated with NGF. The differentiation efficiency was improved by HNP treated cells through activating JNK, p38, and ERK pathways. In addition, the average neurite length was in the order of Sr-HNP > Ba-HNP > Ca-HNP > Mg-HNP. Alkaline earth metal ion-doped HNPs had fluorescence on the percentage of neurite development as following order of Sr-HNP > Mg-HNP > Ca-HNP > Ba-HNP. Compared to previous research, Sr-HNP exhibited highest neurite development effect for PC-12 cells. The alkaline earth metal ion-doped HNPs provide a possibility for novel application of numerous metal hybrid nanomaterials for cell differentiation.

3. Highly uniform 50 nm of HNP was synthesized, modified by GQD and PPy. Herein, GQD/PPy-HNP was applied to encapsulate DEX for electrical stimuli responsive controlled release. The surface coated PPy could be effectively release DEX under electrical stimuli release environment, resulting in the entrapped molecules releasing from the interior of HNPs. To conclude, the fabricated GQD/PPy-HNP possessed lots of superior properties such as biocompatibility and physiological stability, outlining the potential for future biomedical applications.

Compared to the bare HNP, the distinctive release properties of the resulting GQD/PPy-HNP as a controlled release system made it promising for long-term drug delivery and more appropriate for deliver drugs requiring “zero-release” before stimuli. Further study on morphology control of HNP to made it different shape form, optimization of HNP based controlled release system and release properties of larger molecules should be conducted for further application.

In summary, diverse multifunctional hybrid nanomaterials were successfully fabricated and examined their cytotoxicity, and applied as controlled drug delivery agent and neuronal development promoter. First, GO enwrapped HNPs were fabricated for PpIX loading agent and employed for PDT and PTT agent. In case of both of NIR and visible light irradiation condition, the PTT and PDT synergic therapeutic effect has been attained. Second, Mg-HNP, Ca-HNP, Sr-HNP, and Ba-HNPs were used to encapsulating agent for nerve growth factor and further applied as neuronal differentiation enhancer. Sr-HNPs were exceptionally efficient for promoting neuronal development cooperated with nerve growth factor. Third, a stimuli-responsive GQD/PPy-HNPs

were synthesized for use as a bio imaging and drug delivery agent. Each hybrid nanoparticles are intentionally designed and customized of superior performance in specific performance. This study may provide understanding of fabricating various hybrid nanoparticles with multifunctionality and application of hybrid nanoparticles to biomedical application.

References

[1] K. Cho, X. Wang, S. Nie, D. M. Shin, *Clinical cancer research* **2008,** *14*, 1310.

[2] J. Gangwar, B. K. Gupta, S. K. Tripathi, A. K. Srivastava, *Nanoscale* **2015,** *7*, 13313.

[3] C J. Li, T. Zhao, T. Chen, Y. Liu, C. N. Ong, J. Xie, *Nanoscale* **2015,** *7*, 7502.

[4] A. Henglein, *Chemical Reviews* **1989,** *89*, 1861.

[5] H. H. Kung, M. Kung, C. Costello, *Journal of catalysis* **2003,** *216*, 425.

[6] M. Boutonnet, J. Kizling, P. Stenius, G. Maire, *Colloids and Surfaces* **1982,** *5*, 209-225.

[7] L. Quaroni, G. Chumanov, *Journal of the American Chemical Society* **1999,** *121*, 10642.

[8] T. K. Mandal, M. S. Fleming, D. R. Walt, *Nano Letters* **2002,** *2*, 3.

[9] E. Caponetti, L. Pedone, D. C. Martino, V. Panto, V. T. Liveri, *Materials Science and Engineering: C* **2003,** *23*, 531.

[10] S. Gubin, Y. A. Koksharov, *Inorganic materials* **2002,** *38*, 1085.

[11] V. Bakunin, A. Y. Suslov, G. Kuzmina, O. Parenago, A. Topchiev, *Journal of Nanoparticle Research* **2004,** *6*, 273.

[12] Y B. Z. Tang, H. Xu, *Macromolecules* **1999,** *32*, 2569.

[13] H. Duan, M. Kuang, D. Wang, D. G. Kurth, H. Möhwald, *Angewandte Chemie International Edition* **2005,** *44*, 1717.

[14] M. N. Tahir, Functionalized surfaces and surface functionalization of nanomaterials. **2006**

[15] E. Yaghini, A. M. Seifalian, A. J. MacRobert, **2009**.

[16] S. K. Nune, P. Gunda, P. K. Thallapally, Y. –Y. Lin, M. Laird Forrest, C. J. Berkland, *Expert opinion on drug delivery* **2009,** *6*, 1175.

[17] M. Bystrzejewski, S. Cudziło, A. Huczko, H. Lange, G. Soucy, G. Cota-Sanchez, W. Kaszuwara, *Biomolecular engineering* **2007,** *24*, 555.

[18] J. Choi, N. S. Wang, *Nanoparticles in biomedical applications and their safety concerns*. INTECH Open Access Publisher: **2011**.

[19] M. Mahmood, D. Casciano, Y. Xu, A. S. Biris, *Journal of Applied Toxicology* **2012,** *32*, 10.

[20] M. Takahashi, T. Nagao, Y. Imazeki, K. Matsuzaki, H. Minamitani, *Frontiers of Medical and Biological Engineering* **2001,** *11*, 279.

[21] F. Vetrone, R. Naccache, A. J. de la Fuente, F. Sanz-Rodríguez, A. Blazquez-Castro, E. M. Rodriguez, D. Jaque, J. G. Solé, J. A. Capobianco, *Nanoscale* **2010,** *2*, 495.

[22] L. Mocan, C. Matea, O. Mosteanu, T. Pop, C. Puia, T. Mocan, C. Iancu, *Biomaterials* **2017**, *119*, 33.

[23] M. R. Hamblin, L. Y. Chiang, S. Lakshmanan, Y. –Y. Huang, M. Garcia-Diaz, M. Karimi, A. N. de Souza Rastelli, R. Chandran, *Nanotechnology reviews* **2015,** *4*, 359.

[24] H. Kim, S. Mun, Y. Choi, *Journal of Materials Chemistry B* **2013,** *1*, 429.

[25]A. Schroeder, M. S. Goldberg, C. Kastrup, Y. Wang, S. Jiang, B. J. Joseph, C. G. Levins, S. T. Kannan, R. Langer, D. G. Anderson, *Nano letters* **2012,** *12*, 2685.

[26] Z. Xiao, C. Ji, J. Shi, E. M. Pridgen, J. Frieder, J. Wu, O. C. Farokhzad, *Angewandte Chemie* **2012,** *124*, 12023.

[27] E. S. Lee, Z. Gao, D. Kim, K. Park, I. C. Kwon, Y. H. Bae, *Journal of Controlled Release* **2008,** *129*, 228.

[28] E. Koren, A. Apte, A. Jani, V. P. Torchilin, *Journal of controlled release* **2012,** *160*, 264.

[29] E. R. Kandel, J. H. Schwartz, T. M. Jessell, S. A. Siegelbaum, A. Hudspeth, *Principles of neural science*. McGraw-hill New York: **2000**; Vol. 4.

[30] M. J. Mahoney, R. R. Chen, J. Tan, W. M. Saltzman, *Biomaterials* **2005,** *26*, 771.

[31] C. Xie, L. Hanson, W. Xie, Z. Lin, B. Cui, Y. Cui, *Nano letters* **2010,** *10* , 4020.

[32] K. Baranes, N. Chejanovsky, N. Alon, A. Sharoni, O. Shefi, *Biotechnology and bioengineering* **2012,** *109*, 1791.

[33] N. Alon, Y. Miroshnikov, N. Perkas, I. Nissan, A. Gedanken, O. Shefi, *Procedia Engineering* **2013,** *59*, 25.

[34] K. Franze, J. Gerdelmann, M. Weick, T. Betz, S. Pawlizak, M. Lakadamyali, J. Bayer, K. Rillich, M. Gögler, Y.-B. Lu, *Biophysical journal* **2009,** *97*, 1883.

[35] E.-E. Govek, S. E. Newey, L. Van Aelst, *Genes & development* **2005,** *19*, 1.

[36] W. Stöber, A. Fink, E. Bohn, *Journal of colloid and interface science* **1968,** *26*, 62.

[37] G. Bogush, M. Tracy, C. J. Zukoski, *Non-Cryst. Solids* **1988,** *104*, 95.

[38] A. R. Loiola, J. C. R. A. Andrade, J. M. Sasaki, L. R. D. da Silva, *Journal of Colloid and Interface Science* **2012,** *367*, 34.

[39] J. Yao, W. Zhan, X. Liu, Y. Guo, Y. Wang, Y. Guo, G. Lu, *Microporous Mesoporous Mater.* **2012,** *148*, 131.

[40] G. Socrates, *Infrared and Raman characteristic group frequencies : tables and charts*. 3rd ed.; Wiley: Chichester ; New York, **2001**; p xv, 347 p.

[41] N. C. Desai, A. Dodiya, P. Shihora, *Med. Chem. Res.* **2012,** *21*, 1577.

[42]T. Wu, X.-P. Zhang, C.-H. Li, P. Bouř, Y.-Z. Li, X.-Z. You, *Chirality* **2012,** *24*, 451.

[43] J. Avalani, D. Patel, D. Raval, *J. Chem. Sci.* **2012,** *124*, 1091.

[44] A. Ruhal, J.Rana, S. Kumar, A. Kumar, *Cell. Mol. Biol.* **2012,** *58*, 15.

[45] A. Kumar, N. Tarannum, M. Singh, *Mater. Sci. Appl.* **2012,** *3*.

[46] Y. Furukawa, F. Ueda, Y. Hyodo, I. Harada, T. Nakajima, T. Kawagoe, *Macromolecules* **1988,** *21*, 1297.

[47] C. Aggelidou, T. A. Theodossiou, K. Yannakopoulou, *Photochem. Photobiol.* **2013**.

[48] Z. H. Chen, C. Kim, X.-B. Zeng, S. H. Hwang, J. Jang, G. Ungar, *Langmuir* **2012,** *28*, 15350.

[49] C. Kim, S. Kim, W. K. Oh, M. Choi, J. Jang, *Chem.--Eur. J.* **2012,** *18*, 4902.

[50] R. Khandelia, A. Jaiswal, S. S. Ghosh, A. Chattopadhyay, *Small* **2013,** *9*, 3494.

[51] H. L. Tu, Y. S. Lin, H. Y. Lin, Y. Hung, L. W. Lo, Y. F. Chen, C. Y. Mou, *Adv. Mater.* **2009,** *21*, 172.

[52] J. F. Lovell, T. W. Liu, J. Chen, G. Zheng, J. Gao, *Chem. Rev.* **2010,** *110*, 2839.

[53] T. Zhao, H. Wu, S. Q. Yao, Q.-H. Xu, G. Q. Xu, *Langmuir* **2010,** *26*, 14937.

[54] Z. Li, J. Wang, J. Chen, W. Lei, X. Wang, B. Zhang, *Nanotechnology* **2010,** *21*, 115102.

[55] P. Couleaud, V. Morosini, C. Frochot, S. Richeter, L. Raehm, J.-O. Durand, *Nanoscale* **2010,** *2*, 1083.

[56] M. Bottini, S. Bruckner, K. Nika, N. Bottini, S. Bellucci, A. Magrini, A. Bergamaschi, T. Mustelin, *Toxicol. Lett.* **2006,** *160*, 121.

[57]W. Li, W. Lu, Z. Fan, X. Zhu, A. Reed, B. Newton, Y. Zhang, S. Courtney, P. T. Tiyyagura, R. R. Ratcliff, *Journal of materials chemistry* **2012,** *22*, 12701.

[58] S. Orrenius, V. Gogvadze, B. Zhivotovsky, *Annu. Rev. Pharmacol. Toxicol.* **2007,** *47*, 143.

[59] S. Dwivedi, Q. Saquib, A. A. Al-Khedhairy, J. Musarrat, *Toxicology* **2012**.

[60] G. Kanimozhi, N. R. Prasad, S. Ramachandran, K. V. Pugalendi, *Eur. J. Pharmacol.* **2011,** *672*, 20.

[61] Y. Lu, T. Pang, J. Wang, D. Xiong, L. Ma, B. Li, Q. Li, S. Wakabayashi, *Biochem. Biophys. Res. Commun.* **2008,** *377*, 441.

[62] M. Choi, C. Kim, S. O. Jeon, K. S. Yook, J. Y. Lee, J. Jang, *Chemical Communications* **2011,** *47*, 7092.

[63] L. Zhao, Y. Zhao, Y. Han, *Langmuir* **2010,** *26*, 11784.

[64]I. Pellejero, M. Urbiztondo, M. Villarroya, J. Sesé, M. Pina, J. Santamaría, *Microporous and Mesoporous Materials* **2008,** *114*, 110.

[65] .-F. Chen, H.-M. Ding, J.-X. Wang, L. Shao, *Biomaterials* **2004,** *25*, 723.

[66] W. Zhao, H. Chen, Y. Li, L. Li, M. Lang, J. Shi, *Advanced Functional Materials* **2008,** *18*, 2780.

[67] Y. Zhu, T. Ikoma, N. Hanagata, S. Kaskel, *Small* **2010,** *6*, 471.

[68] Y. Chen, H. Chen, D. Zeng, Y. Tian, F. Chen, J. Feng, J. Shi, *ACS nano* **2010,** *4*, 6001.

[69] F. Garbassi, L. Balducci, P. Chiurlo, L. Deiana, *Applied surface science* **1995,** *84*, 145.

[70] T. Nguyen, S. Lefrant, *Journal of Physics: Condensed Matter* **1989,** *1*, 5197.

[71] C. Greenlief, J. White, C. Ko, R. Gorte, *The Journal of Physical Chemistry* **1985,** *89*, 5025.

[72] X. Li, J. Fu, M. Steinhart, D.-H. Kim, W. Knoll, *Bulletin of the Korean Chemical Society* **2007,** *28*, 1015.

[73] F. Tian, Z. Wu, Q. Chen, Y. Yan, G. Cravotto, Z. Wu, *Applied Surface Science* **2015,** *351*, 104.

[74] S. H. Chuang, R. H. Gao, D. Y. Wang, H. P. Liu, L. M. Chen, M. Y. Chiang, *Journal of the Chinese Chemical Society* **2010,** *57*, 932.

[75] A. K. L. Sajjad, S. Shamaila, J. Zhang, *Journal of hazardous materials* **2012,** *235*, 307.

[76] M. Viviani, M. Buscaglia, P. Nanni, R. Parodi, G. Gemme, A. Dacca, *Journal of the European Ceramic Society* **1999,** *19*, 1047.

[77] M. Houmard, D. Vasconcelos, W. Vasconcelos, G. Berthomé, G. J. Joud, M. Langlet, *Surface Science* **2009,** *603*, 2698.

[78] Y. Yang, M. Liu, Y. Gu, S. Lin, F. Ding, X. Gu, *Cell biology international* **2009,** *33*, 352.

[79] J. Schimmelpfeng, K.-F. Weibezahn, H. Dertinger, *Journal of neuroscience methods* **2004,** *139*, 299.

[80] Y. Zhang, S. F. Ali, E. Dervishi, Y. Xu, Z. Li, D. Casciano, A. S. Biris, *Acs Nano* **2010,** *4*, 3181.

[81] G. Esposito, D. De Filippis, R. Carnuccio, A. A. Izzo, T. Iuvone, *Journal of molecular medicine* **2006,** *84*, 253.

[82] M. Giorgio, E. Migliaccio, F. Orsini, D. Paolucci, M. Moroni, C. Contursi, G. Pelliccia, L. Luzi, S. Minucci, M. Marcaccio, *Cell* **2005,** *122*, 221.

[83] A. Grzelak, B. Rychlik, G. Bartosz, *Free Radical Biology and Medicine* **2001,** *30*, 1418.

[84]N. M. Idris, M. K. Gnanasammandhan, J. Zhang, P. C. Ho, R. Mahendran, Y. Zhang, *Nature medicine* **2012,** *18*, 1580.

[85] P. Mroz, A. Pawlak, M. Satti, H. Lee, T. Wharton, H. Gali, T. Sarna, M. R. Hamblin, *Free Radical Biology and Medicine* **2007,** *43*, 711.

[86] H. Guo, H. Qian, N. M. Idris, Y. Zhang, *Nanomedicine: Nanotechnology, Biology and Medicine* **2010,** *6*, 486.

[87] K. A. Kristiansen, P. E. Jensen, I. M. Møller, A. Schulz, *Physiologia plantarum* **2009,** *136*, 369.

[88] W. Zhu, F. Masood, J. O'Brien, L. G. Zhang, *Nanomedicine: Nanotechnology, Biology and Medicine* **2015,** *11*, 693.

[89] S. P. Squinto, T. N. Stitt, T. H. Aldrich, S. Davis, S. M. Blanco, C. RadzieJewski, D. J. Glass, P. Masiakowski, M. E. Furth, D. M. Valenzuela, *Cell* **1991,** *65*, 885.

[90] M. Sendtner, G. Pei, M. Beck, U. Schweizer, S. Wiese, *Cell and tissue research* **2000,** *301*, 71.

[91] D. Zhou, Y. Ito, *Rsc Advances* **2013,** *3*, 11095.

[92] N. Kobayashi, H. Kiyama, M. Tohyama, *Molecular brain research* **1994,** *21*, 9.

[93] P. Geldhof, A. Visser, D. Clark, G. Saunders, C. Britton, J. Gilleard, M. Berriman, D. Knox, *Parasitology* **2007,** *134*, 609.

[94] B. Ault, R. Evans, A. Francis, D. Oakes, J. Watkins, *The Journal of Physiology* **1980,** *307*, 413.

[95]G. R. Hamilton, S. K. Sahoo, S. Kamila, N. Singh, N. Kaur, B. W. Hyland, J. F. Callan, *Chemical Society Reviews* **2015,** *44*, 4415.

[96] F. Horkay, I. Tasaki, P. J. Basser, *Biomacromolecules* **2001,** *2*, 195. [97] O. Veiseh, R. Lauger, *Nature* **2015**, 524, 39.

[97] S. Akine, T. Taniguchi, T. Saiki, T. Nabeshima, *Journal of the American Chemical Society* **2005,** *127*, 540.

[98] G. Rudenko, L. Henry, K. Henderson, K. Ichtchenko, M. S. Brown, J. L. Goldstein, J. Deisenhofer, *Science* **2002,** *298*, 2353.

[99]J. C. Dewan, B. Mikami, M. Hirose, J. C. Sacchettini, *Biochemistry* **1993,** *32*, 11963.

[100] R.-R. Ji, T. A. Samad, S.-X. Jin, R. Schmoll, C. J. Woolf, *Neuron* **2002,** *36*, 57.

[101] M. Schäfers, C. I. Svensson, C. Sommer, L. S. Sorkin, *The Journal of neuroscience* **2003,** *23*, 2517.

[102] J. K. Wong, H. H. Le, A. Zsarnovszky, S. M. Belcher, *The Journal of*

neuroscience **2003,** *23*, 4984.

[103] D. S. Park, S. E. Farinelli, L. A. Greene, *Journal of Biological Chemistry* **1996,** *271*, 8161.

[104] C. D. Cone, C. M. Cone, *Science* **1976,** *192*, 155.

[105] J. Lee, S. H. Hwang, J. Yun, J. Jang, *ACS applied materials & interfaces* **2014,** *6*, 15420.

[106] L. Chen, C. X. Guo, Q. Zhang, Y. Lei, J. Xie, S. Ee, Q. Guai, Q. Song, Q. C. M. Li, *ACS applied materials & interfaces* **2013,** *5*, 2047.

[107] K. Ramanathan, M. A. Bangar, M. Yun, W. Chen, N. V. Myung, A. Mulchandani, *Journal of the American Chemical Society* **2005,** *127*, 496.

[108] J. S. Kim, W. J. Kim, N. Cho, S. Shukla, H. Yoon, J. Jang, P. N. Prasad, T.-D. Kim, K.-S. Lee, *Journal of nanoscience and nanotechnology* **2009,** *9*, 6957.

[109] R. Rajagopalan, J. O. Iroh, *Applied surface science* **2003,** *218*, 58.

[110] S. Carquigny, J.-B. Sanchez, F. Berger, B. Lakard, F. Lallemand, *Talanta* **2009,** *78*, 199.

[111] V. Chandra, S. U. Yu, S. H. Kim, Y. S. Yoon, D. Y. Kim, A. H. Kwon, M. Meyyappan, K. S. Kim, *Chemical communications* **2012,** *48*, 735.

[112] S. Bose, T. Kuila, M. E. Uddin, N. H. Kim, A. K. Lau, J. H. Lee, *Polymer* **2010,** *51*, 5921.

[113] D. Zhang, X. Zhang, Y. Chen, P. Yu, C. Wang, Y. Ma, *Journal of Power Sources* **2011,** *196*, 5990.

[114] S. Sahoo, G. Karthikeyan, G. C. Nayak, C. K. Das, *Synthetic Metals* **2011,** *161*, 1713.

[115] S. Biswas, L.T. Drzal, *Chemistry of Materials* **2010,** *22*, 5667.

[116] M. Omastova, M. Trchova, J. Kovářová, J. Stejskal, *Synthetic Metals* **2003,** *138*, 447.

[117] X. Yang, Y. Lu, *Materials letters* **2005,** *59*, 2484.

[118] P. Si, H. Chen, P. Kannan, D.-H. Kim, *Analyst* **2011,** *136*, 5134.

[119] C. Bora, S. Dolui, *Polymer* **2012,** *53*, 923.

[120] S. Bose, N. H. Kim, T. Kuila, K.-T. Lau, J. H. Lee, *Nanotechnology* **2011,** *22*, 295202.

[121] J. Shen, Y. Zhu, X. Yang, C. Li, *Chemical Communications* **2012,** *48*, 3686.

[122] S. Zhu, J. Zhang, C. Qiao, S. Tang, Y. Li, W. Yuan, B. Li, L. Tian, F. Liu, R. Hu, *Chemical communications* **2011,** *47*, 6858.

[123] Y. Li, Y. Hu, Y. Zhao, G. Shi, L. Deng, Y. Hou, L. Qu, *Advanced Materials* **2011,** *23*, 776.

[124] Z. M. Markovic, B. Z. Ristic, K. M. Arsikin, D. G. Klisic, L. M. Harhaji-Trajkovic, B. M. Todorovic-Markovic, D. P. Kepic, T. K. Kravic-Stevovic, S. P. Jovanovic, M. M. Milenkovic, *Biomaterials* **2012,** *33*, 7084.

[125] X. Yuan, Z. Liu, Z. Guo, Y. Ji, M. Jin, X. Wang, *Nanoscale research letters* **2014,** *9*, 1

[126] C. Liu, P. Zhang, X. Zhai, F. Tian, W. Li, J. Yang, Y. Liu, H. Wang, W. Wang, W. Liu, *Biomaterials* **2012,** *33*, 3604.

[127] L.-Z. Fan, J. Maier, *Electrochemistry communications* **2006,** *8*, 937.

[128] R. Sharma, A. Rastogi, S. Desu, *Electrochemistry Communications* **2008,** *10*, 268.

[129] J. Ge, E. Neofytou, T. J. Cahill, R. E. Beygui, R. N. Zare, *ACS nano* **2011,** *6*, 227.

[130] M. R. Abidian, D. H. Kim, D. C. Martin, *Advanced materials* **2006,** *18*, 405.

[131] S. Mura, J. Nicolas, P. Couvreur, *Nature materials* **2013,** *12*, 991.

[132] P. M. George, D. A. LaVan, J. A. Burdick, C. Y. Chen, E. Liang, R. Langer, *Advanced Materials* **2006,** *18*, 577.

[133] G. Jeon, S. Y. Yang, J. Byun, J. K. Kim, *Nano letters* **2011,** *11*, 1284..

[134] S. Sirivisoot, R. Pareta, T. J. Webster, *Nanotechnology* **2011,** *22*,

085101.

[135] M. Sharma, G.I. Waterhouse, S. W. Loader, S. Garg, D. Svirskis, *International journal of pharmaceutics* **2013,** *443*, 163.

[136] T. Hickey, D. Kreutzer, D. Burgess, F. Moussy, *Biomaterials* **2002,** *23*, 1649.

[136] R. Dus, R. Nowakowski, E. Nowicka, *J. Alloys Compd.* **2005**, 404-406, 284.

[137] L. Leprince, A. Dogimont, D. Magnin, S. Demoustier-Champagne, *Journal of Materials Science: Materials in Medicine* **2010,** *21*, 925.

[138] T. Murakami, K. Ajima, J. Miyawaki, M. Yudasaka, S. Iijima, K. Shiba, *Molecular pharmaceutics* **2004,** *1*, 399.

[139] T. Ito, L. P. Fraser, Y. Yeo, C. B. Highley, E. Bellas, D. S. Kohane, *Biomaterials* **2007,** *28*, 1778.

[140] D. Chauhan, G. Li, K. Podar, T. Hideshima, P. Neri, D. He, N. Mitsiades, P. Richardson, Y. Chang, J. Schindler, *Cancer research* **2005,** *65*, 8350.

[141] P. M. Voorhees, Q. Chen, G. W. Small, D. J. Kuhn, S. A. Hunsucker, J. A. Nemeth, R. Z. Orlowski, *British journal of haematology* **2009,** *145*, 481.

[142] X. Chen, T. Murakami, J. J. Oppenheim, O. Howard, *European journal of immunology* **2004,** *34*, 859.

[143] E. Laane, K. P. Tamm, E. Buentke, K. Ito, P. Khahariza, J. Oscarsson, M. Corcoran, A. Björklund, K. Hultenby, J. Lundin, *Cell Death & Differentiation* **2009,** *16*, 1018.

국문초록

최근 나노 크기의 단일시스템 안에서 다양한 요소들을 도입하는 연구가 생명과학 분야에서 많은 관심을 받고 있다. 기존의 물질이나 단일 요소로 구성된 나노 물질에 비해서 복합 나노 물질은 다양한 분야에서 매우 뛰어난 성능을 발휘하며 향상된 기능성을 가지고 있다는 장점이 있다. 이에 나노 기술의 발전과 함께 복합 나노 물질을 제조하는 연구가 활발히 진행되고 있다. 나노 입자는 이런 복합성을 가질 수 있는 가장 기본적인 구조이며, 구성에 따라서 복합 나노 입자는 다른 나노 구조체에 비해 세포 내에 가장 많이 도입될 수 있는 장점을 가질 수 있다. 하지만, 생명과학 분야에 적합한 복합 나노 입자를 제조하는 연구에 관한 보고는 여전히 부족한 실정이다.

본 연구에서는 기능성이 부여된 복합 나노입자를 제조하여 세포독성을 평가하고, 제조한 입자를 약물전달시스템과 신경세포 분화 촉진에 응용하였다. 본 학위논문은 그래핀으로 감싼 중공구조 나노입자를 이용한 광촉매물질의 전달 응용, 알칼리 토금속이 도핑된 실리카/티타니아 나노입자를 사용한 세포분화 촉진 응용, 그리고 나노물질의 표면에 폴리피롤이 코팅된 입자를 이용한 약물

전달과 바이오 이미징 응용, 이렇게 총 세개의 부분으로 구성되어 있다.

내부에 광촉매가 도입된 그래핀으로 감싼 중공구조 나노입자는 초음파 매개 에칭/재증착 방법과 용매치환법, 그리고 실랑 커플링 처리를 통해 제조하였다. 그래핀으로 감싼 중공구조 나노입자는 높은 생체친화성을 가지고 있으며, 세포 내부로 광촉매를 효율적으로 전달할 수 있는 매개체로 응용되었다. 또한, 제조한 나노입자는 적외선과 가시광선 파장의 빛을 조사함에 따라 뛰어난 광역동치료와 광열치료 효과를 발휘하였다.

알칼리 토금속이 도핑된 실리카/티타니아 나노입자는 화학적 환원방법을 통하여 제조하였다. 네 가지 다른 종류의 알칼리 토금속 (마그네슘, 칼슘, 스트론튬, 그리고 바륨) 이 도핑된 실리카/티타니아 나노입자는 신경 분화 촉진제로 이용되었으며, 나아가 신경성장인자의 전달체로 사용하였다. 도핑된 알칼리 토금속의 종류에 따라 다른 세포분화 촉진효과를 관찰 할 수 있었으며, 이중 스트론튬이 도핑된 실리카/티타니아 나노입자에서 뛰어난 분화 촉진 효과를 관찰하였다.

그래핀 양자점과 폴리피롤이 도입된 실리카/티타니아 중공구조 나노입자는 에멀젼 상에서 산화중합을 통해 제조하였다. 낮은 독성을 가지고 있는 그래핀 양자점과 폴리피롤이 표면에 코팅된

나노입자는 생체 내에서 효과적으로 세포를 이미징 하는 에이전트로 적용이 될 수 있으며 동시에 전기적 자극에 감응하는 약물방출 효과를 보여주었다.

본 학위 논문에서 기능성 복합 나노입자를 제조하는 다양한 방법과 생명과학분야 응용 가능성에 대해 평가하였다. 본 학위 논문에서 제조된 복합 나노 입자들은 약물전달매개체, 신경분화 촉진제, 그리고 바이오 이미징과 같은 생명과학분야에 응용하였다. 본 입자들은 각각의 응용에 적합하고 최적의 성능을 낼 수 있도록 디자인되고 제조되었다. 이런 결과들은 기능성 복합 나노 입자를 제조하고, 이들을 생명과학분야에 적용하는 것에 관한 정보들을 제공하게 될 것이다.

주요어: 복합 나노입자; 세포 독성; 신경 분화; 약물전달; 세포 이미징
학 번: 2014-30296